Title

Multihadronic events at Ec.m.=29 GeV and predictions of QCD models from Ec.m.=29 GeV to Ec.m.=93 GeV

Journal

Physical Review D, 37(1)

ISSN

2470-0010

Authors

Petersen, A
Abrams, G
Adolphsen, CE
et al.

Publication Date

1988

DOI

10.1103/physrevd.37.1

PHYSICAL REVIEW D

PARTICLES AND FIELDS

THIRD SERIES, VOLUME 37, NUMBER 1 1 JANUARY 1988

Multihadronic events at $E_{c.m.}=29$ GeV and predictions of QCD models from $E_{c.m.}=29$ GeV to $E_{c.m.}=93$ GeV

A. Petersen,[α] G. Abrams,[β] C. E. Adolphsen,[γ] C. Akerlof,[δ] J. P. Alexander,[α] M. Alvarez,[ε,(a)] D. Amidei,[β,(b)] A. R. Baden,[β,(c)] J. Ballam,[α] B. C. Barish,[ζ] T. Barklow,[α] B. A. Barnett,[η] J. Bartelt,[α] D. Blockus,[θ] G. Bonvicini,[δ] A. Boyarski,[α] J. Boyer,[β] B. Brabson,[θ] A. Breakstone,[ι] J. M. Brom,[θ] F. Bulos,[α] P. R. Burchat,[γ] D. L. Burke,[α] F. Butler,[β] F. Calvino,[ε,(a)] R. J. Cence,[ι] J. Chapman,[δ] D. Cords,[α] D. P. Coupal,[α] H. C. DeStaebler,[α] D. E. Dorfan,[γ] J. M. Dorfan,[α] P. S. Drell,[β] G. J. Feldman,[α] E. Fernandez,[ε,(a)] R. C. Field,[α] W. T. Ford,[ε] C. Fordham,[α] R. Frey,[δ] D. Fujino,[α] K. K. Gan,[α] G. Gidal,[β] L. Gladney,[α,(d)] T. Glanzman,[α] M. S. Gold,[β] G. Goldhaber,[β] L. Golding,[β,(e)] A. Green,[α,(f)] P. Grosse-Wiesmann,[α] J. Haggerty,[β,(g)] G. Hanson,[α] R. Harr,[β] F. A. Harris,[ι] C. M. Hawkes,[ζ] K. Hayes,[α] D. Herrup,[β] C. A. Heusch,[γ] T. Himel,[α] M. Hoenk,[ζ] R. J. Hollebeek,[α,(d)] D. Hutchinson,[α] J. Hylen,[η] W. R. Innes,[α] M. Jaffre,[β] J. A. Jaros,[α] I. Juricic,[β] J. A. Kadyk,[β] D. Karlen,[α] J. Kent,[γ] S. R. Klein,[α] A. Koide,[ι,(h)] W. Koska,[δ] W. Kozanecki,[α] A. J. Lankford,[α] R. R. Larsen,[α] B. W. LeClaire,[α] M. E. Levi,[α] Z. Li,[ζ] A. M. Litke,[γ] N. S. Lockyer,[α,(d)] C. Matteuzzi,[α,(i)] J. A. J. Matthews,[η] D. I. Meyer,[δ] B. D. Milliken,[ζ] K. C. Moffeit,[α] L. Müller,[α,(j)] J. Nash,[α] M. E. Nelson,[ζ] D. Nitz,[δ] H. Ogren,[θ] R. A. Ong,[α] K. F. O'Shaughnessy,[α] S. I. Parker,[ι] C. Peck,[ζ] M. L. Perl,[α] M. Petradza,[δ] F. C. Porter,[ζ] P. Rankin,[α] B. Richter,[α] K. Riles,[α] P. C. Rowson,[β,(k)] D. R. Rust,[θ] H. F. W. Sadrozinski,[γ] T. Schaad,[κ,(l)] T. L. Schalk,[γ] H. Schellman,[β,(b)] W. B. Schmidke,[β] A. S. Schwarz,[γ] A. Seiden,[γ] P. D. Sheldon,[β,(m)] J. G. Smith,[ε] A. Snyder,[θ] E. Soderstrom,[ζ] D. P. Stoker,[η] R. Stroynowski,[ζ] R. Thun,[δ] G. H. Trilling,[β] R. Tschirhart,[δ] C. de la Vaissiere,[β,(n)] R. Van Kooten,[α] H. Veltman,[δ,(f)] P. Voruganti,[α] S. R. Wagner,[ε] P. Weber,[ε] A. J. Weinstein,[γ] A. Weir,[ζ] S. Weisz,[γ,(i)] S. L. White,[ε] E. Wicklund,[ζ] D. R. Wood,[β] D. Y. Wu,[ζ] and J. M. Yelton[α,(o)]

[α]*Stanford Linear Accelerator Center, Stanford University, Stanford, California 94305*

[β]*Lawrence Berkeley Laboratory and Department of Physics, University of California, Berkeley, California 94720*

[γ]*University of California, Santa Cruz, California 95064*

[δ]*University of Michigan, Ann Arbor, Michigan 48109*

[ε]*University of Colorado, Boulder, Colorado 80309*

[ζ]*California Institute of Technology, Pasadena, California 91125*

[η]*Johns Hopkins University, Baltimore, Maryland 21218*

[θ]*Indiana University, Bloomington, Indiana 47405*

[ι]*University of Hawaii, Honolulu, Hawaii 96822*

[κ]*Harvard University, Cambridge, Massachusetts 02138*

(Received 14 May 1987)

Multihadronic e^+e^- annihilation events at a center-of-mass energy of 29 GeV have been studied with both the original (PEP 5) Mark II and the upgraded Mark II detectors. Detector-corrected distributions from global shape analyses such as aplanarity, Q_2-Q_1, sphericity, thrust, minor value, oblateness, and jet masses, and inclusive charged-particle distributions including x, rapidity, $p_\perp$, and particle flow are presented. These distributions are compared with predictions from various multihadron event models which use leading-logarithmic shower evolution or QCD matrix elements at the parton level and string or cluster fragmentation for hadronization. The new generation of parton-shower models gives, on the average, a better description of the data than the previous parton-shower models. The energy behavior of these models is compared to existing e^+e^- data. The predictions of the models at a center-of-mass energy of 93 GeV, roughly the expected mass of the Z^0, are also presented.

I. INTRODUCTION

Hadronic final states in high-energy e^+e^- annihilation have been studied in great detail during the past decade. Unlike hadron-hadron collisions, where spectators which can mask the process of interest are present, e^+e^- annihilation is an ideal place to study strong interactions. All the available data support the assumption that the underlying process can be described by the primary production of a pair of quarks, $e^+e^- \to q\bar{q}$, which then fragment into the observed hadrons. The steps in between are, as yet, not totally understood, but today it is generally accepted that the hard processes involved can be described by the theory of quantum chromodynamics (QCD). This implies that the primary quarks radiate gluons as they move apart. The subsequent transformation of the outgoing partons into stable hadrons is still an unsolved, nonperturbative phenomenon. To cover this area, several fragmentation models have been developed over the past years, giving experimenters some useful tools with which to correct their data and to unravel the underlying parton structure. In addition, these models might help us to understand better the long-range behavior of the strong interaction.

In this paper we present general properties of hadronic final states produced by e^+e^- annihilation at a center-of-mass energy of $E_{\text{c.m.}}=29$ GeV, measured with the original (PEP 5) and the upgraded Mark II detector at the SLAC storage ring PEP.

Although these results stand on their own, it will be interesting to compare them with data which will be taken in the 90-GeV region by experiments at the SLAC Linear Collider (SLC) to see how these observables evolve over this energy range. It is also important to see whether any of the "QCD plus fragmentation" models are able to describe the data over such a wide energy range. This also implies that we have to be able to understand the "old physics" as being the background to possible new physics at energies near the Z^0 mass. The aim of this paper can be summarized as follows: to compare the corrected distributions from the original Mark II and the upgraded Mark II detector, to test how well the existing QCD models are able to describe the data, and to present predictions of these models at $E_{\text{c.m.}}=93$ GeV without changing the parameters which are optimized at $E_{\text{c.m.}}=29$ GeV. To allow someone to test a new model by comparing it with these data, we include all the measured distributions in tables.

After a short introduction to the QCD models in the second section, we give a brief discussion of the apparatus and the particle and event selection in Secs. III and IV. The definitions of the observables used in this analysis are given in Sec. V. Section VI explains how the data are corrected, and Sec. VII makes a comparison between the two Mark II data sets. Section VIII compares the models with the data and in Sec. IX the energy dependence of the average values of the observables is compared with data from this and other experiments. The predictions of the models at energies near the Z^0 mass are presented in Sec. X.

II. QCD PLUS FRAGMENTATION MODELS

There are several models for multihadron production currently available and, since their authors are continually working to improve them, it is sometimes difficult to keep track of the latest developments. With respect to the QCD calculations, the models can be divided into two groups: those in which partons are produced according to the second order in α_s QCD matrix elements and those in which they are produced by leading-logarithmic parton-shower evolution.

For the fragmentation of the partons into hadrons there are three main schemes available: independent fragmentation[1] (IF), string fragmentation[2] (SF), and cluster fragmentation[3] (CF). The independent fragmentation scheme is strongly disfavored by the data in certain regions,[4] so it will not be discussed further here. We will restrict ourselves mainly to the model of Webber[5] (version 4.1), the Lund model[6] (JETSET 6.3), and that of Gottschalk and Morris[7] (CALTECH II). For all the models the purely weak effects which are important at the Z^0 energies and the electroweak interferences on the total cross section, flavor composition, and angular distributions are taken into account. The simulations of the weak effects are taken from the Lund generator.[6]

The parameter values of the models given below are the results of investigations of the multidimensional parameter space by fits to the distributions of the data given in this paper. A total systematic optimization procedure was not used, since the variety of data sets used did not cover the event topologies uniformly and may bias the χ^2 values from the fits.

A. The Webber model

The Webber model uses the leading-logarithmic parton-shower evolution and includes coherence effects by angular ordering.[8] The highly excited $q\bar{q}$ system evolves in the first phase (early times) into a system of partons with lower virtuality by radiating gluons and producing new $q\bar{q}$ pairs according to the leading-logarithmic QCD probabilities. If the virtual mass of a given parton reaches a certain cutoff (m_g), the evolution stops for this parton. At the end of the shower the final gluons are forced to split into $q\bar{q}$ pairs by the same mechanism. Neighboring $q\bar{q}$ pairs along the color flux lines are combined to form colorless clusters. These clusters decay according to a phase-space model into one or two particles which can be stable particles or resonances.

At the beginning of the evolution, the initial system is boosted perpendicular to the primary quark direction such that all partons are produced in one hemisphere. This provides an elegant way of handling the angular ordering, but has the problem that the total center-of-mass energy of the system can be found only after the whole shower evolution of the event, and the final-state system depends partly on the way it is boosted.[9] Another problem is the existence of very massive clusters which cannot be allowed to decay isotropically.[10] A stringlike scheme is used to break these clusters into two smaller

TABLE I. The parameters for the Webber model.

Parameter	Range tested	Best value
Λ_{LLA} QCD scale (GeV)	0.15–0.3	0.2
m_g cutoff for further parton evolution (GeV)	0.6–0.85	0.75
m_{cl} cutoff for string breaking of clusters (GeV)	2.5–3.8	3.0

clusters, each of which may break further if massive enough. Unfortunately this heavy-cluster decay produces more particles from a given cluster mass than the parton shower does from a primary gluon of the same invariant mass. This leads to the strange situation that an increase of the QCD scale Λ_{LLA} where LLA denotes the leading-logarithmic approximation results in more produced gluons but no increase in the number of final-state hadrons.[11]

An important change in version 4.1 is the new treatment of the first splitting of the virtual photon into the primary $q\bar{q}$ pair. This is now performed according to the Altarelli-Parisi splitting function[12] $P(z)=\frac{3}{2}[z^2+(1-z)^2]$, where z is the fraction of energy assigned to one quark. It leads to a more asymmetric parton distribution in z which produces more 3-jet events, in better agreement with the data than the older version 2.0.

Table I shows the three important parameters of the model with the range we tested for the optimization and the best values for describing the data. The additional parameters were used with the default values in the generator. However, the Lund decay routines were used for charmed meson decays.

It should be pointed out that the Λ_{LLA} value in a leading logarithmic evolution cannot be directly correlated to the $\Lambda_{\overline{MS}}$ value estimated from the first- or second-order matrix-element calculation. ($\overline{MS}$ denotes the modified minimal-subtraction scheme.)

B. The Lund model

The Lund model provides us with two options for parton generation: a second-order matrix-element calculation (Lund MA) and a leading-logarithmic parton shower (Lund shower). At low $E_{c.m.}$ $O(\alpha_s^2)$ matrix elements[13] seem to be adequate, but at SLC or CERN LEP energies the production of at most four partons will probably be insufficient. Indications at DESY PETRA and PEP energies show that these data also demand higher parton multiplicities[14] than produced by Lund MA. Another problem is implied by the y_{min} cutoff. The production of two-, three-, and four-parton final states is determined by α_s and the lower cutoff y_{min}. If the value $M_{ij}^2/E_{c.m.}^2$ of any pair of partons i and j of an event is less than y_{min}, then these two partons are combined to one parton. Using the same y_{min} value at different center-of-mass energies implies a fragmentation scheme which has to be Q^2 dependent. Almost none of the fragmentation schemes is Q^2 dependent. To compensate for this a cutoff defined in M_{ij}^2 should be used, but covering an energy range from 30 to 90 GeV confronts one then with the following problem: a M_{ij}^2 cutoff which describes the data well at 30 GeV leads at high $E_{c.m.}$ to a $3+4$-parton rate which exceeds the total cross section, and a cutoff which is well defined at 90 GeV results in no agreement with data at 30 GeV. Because of this we will

TABLE II. (a) The parameters for the Lund shower model. (b) The parameters for the Lund MA model.

Parameter	Range tested	Best value
(a)		
Λ_{LLA} QCD scale (GeV)	0.2–0.6	0.4
Q_0 cutoff for parton evolution (GeV)	1.0–2.0	1.0
A fragmentation-function parameter	0.1–0.5	0.45
B fragmentation-function parameter	0.8–1.2	0.9
σ_q parameter of the Gaussian (Ref. 15) $p_\perp$(GeV)/c	0.18–0.27	0.23
(b)		
$\Lambda_{\overline{MS}}$ QCD scale (GeV)	0.3–0.6	0.5
y_{min} cutoff for combining partons	Fixed	0.015
A fragmentation-function parameter	0.5–1.3	0.9
B fragmentation-function parameter	0.5–1.3	0.7
σ_q parameter of the Gaussian (Ref. 15) $p_\perp$(GeV)/c	0.2–0.3	0.265

use in this paper a fixed $y_{\min}$ cutoff for all energies knowing that the fragmentation scheme had to be Q^2 dependent to get the right scaling.

This problem does not occur in the parton-shower evolution where a fixed cutoff Q_0 is used, rather than a scaled one. In the parton-shower option in the Lund model the evolution proceeds in the c.m. system. The angular ordering is imposed by a rejection technique at each step. For the first branch on each side no angular ordering is taken, instead the matrix elements are used as a guideline here.

At the end of the parton production, string fragmentation[2] is used in both options. A string is stretched from a quark via gluons to an antiquark. Breaks in the string result in the production of additional $q\bar{q}$ pairs. The breaking can be understood as a tunneling phenomenon, automatically providing a suppression of heavy flavor production and a Gaussian transverse-momentum spectrum.

The relevant parameters for the Lund shower option are given in Table II(a) and for the Lund MA in Table II (b). The other parameters are used with the default values in JETSET 6.3 except that the results on D^0 and D^+ branching ratios from Mark III are taken into account.[16]

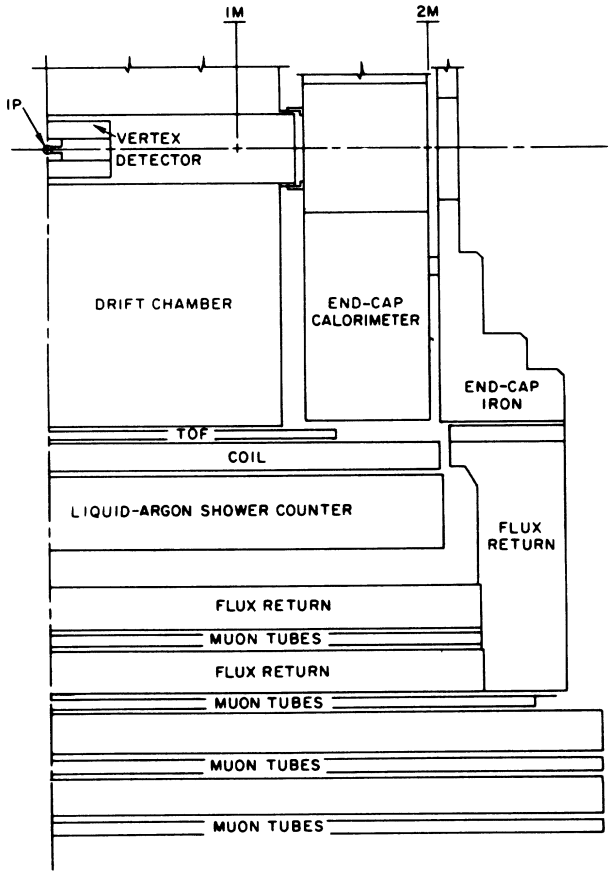

FIG. 1. A schematic plane view of the upgraded Mark II detector.

The range of the parameters given in the tables was covered by roughly 40 different parameter sets. An increase of Λ by 0.1 GeV leads to the production of $\simeq 0.4$ more charged particles, whereas increasing σ_q by 50 MeV/c reduces the average number of charged particles by $\simeq 0.5$. This, and the fact that the parameters A and B are highly correlated, reduces the variation in the parameter space quite drastically if one demands the average multiplicity to be between 12.5 and 13.5 to describe the measured data. The comparisons with the data show that the values for Q_0 and $y_{\min}$ should be made as small as possible to get sufficient gluon radiation. The best values given are more or less the kinematic limits in the generators.

C. The CALTECH II model

The CALTECH II model of Gottschalk and Morris starts with a leading-logarithmic parton shower, where the evolution proceeds in the c.m. system. The coherence effect by angular ordering is imposed by rejection techniques at each step. As with the Lund model, a reweighting of the first splitting according to the matrix element is used. At the end of the shower the quarks and gluons are replaced by color strings which break up into substrings according to the Artru-Mennessier scheme.[17] It implies a uniform string breaking with no mass-shell constraints, in contrast with the Lund scheme, and it has no limited transverse-momentum production during the string breaking. Substrings below a certain cutoff are treated as colorless clusters which decay according to a phase-space model optimized with low-energy data.

The important parameters are given in Table III, whereas for the additional parameters the default values are chosen. The parameters t_0 and $w_{\min}$ have been fixed to the default values according to the results in Ref. 7.

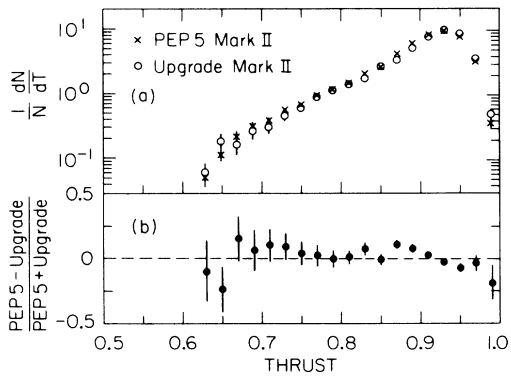

FIG. 2. Comparison of the corrected distributions from the PEP 5 Mark II detector and the upgraded one, (a) thrust, (b) the ratio (upgrade − PEP 5)/(upgrade + PEP 5) for the thrust distribution.

TABLE III. The parameters for the CALTECH II model.

Parameter	Range tested	Best value
Λ_{LLA}QCD scale (GeV)	0.3–0.6	0.5
t_0 cutoff for further parton evolution (GeV^2)	Fixed	2.0
ρ string breaking parameter (GeV^{-2})	1.4–2.4	1.6
w_{max} cluster decay parameter (GeV)	1.9–3.0	2.2
w_{min} cluster decay parameter (GeV)	Fixed	0.25

III. APPARATUS

Our data can be divided into two subsamples which are taken with two very different detector configurations. The PEP 5 Mark II detector collected a data sample corresponding to an integrated luminosity of 210 pb^{-1}. In this analysis we used only the high-performance runs of the apparatus which contain $\frac{2}{3}$ of the amount of data taken with that detector. The upgraded version of the Mark II detector collected a data sample at PEP with an integrated luminosity of 30 pb^{-1}. The upgrade was designed to improve the match of the Mark II detector to the requirements of the physics at the Z^0 energy, and the operation at PEP was primarily to provide a check for the new components before the SLC was turned on.

The PEP 5 Mark II detector has been described in detail elsewhere.[18] For most of the data, the magnetic field of the old coil was limited to 2.3 kG. The components relevant for this analysis are both the inner and main drift chambers which are used for charged-track reconstruction and provide a momentum resolution of $(\delta p/p)^2=0.025^2+(0.01p)^2$ (p is the particle momentum in GeV/c), and the central region lead–liquid-argon calorimeter modules,[19,20] which are 14 radiation lengths in depth and detect photons by their electromagnetic showers. The calorimeter has an energy resolution of $\delta E/E=0.14/\sqrt{E}$ (E in GeV).

The design of the upgraded Mark II detector is described in Ref. 20. A schematic view of it is given in Fig. 1. The new coil provides a magnetic field of 4.5 kG. The new central drift chamber[21] is based on a multi-sense-wire cell of the jet chamber type. Its outer radius is limited by the time-of-flight counters and the magnet flux-return iron as in the old detector. Each cell contains six sense wires (spaced by 8.33 mm), staggered by ± 380 μm from the cell axis to provide left-right ambiguity resolution. Radially the whole chamber consists of twelve layers of cells providing 72 measurements per track. The even-numbered layers have their wires at a stereo angle of $\pm 3.8°$ to provide position measurements along the z direction. The chamber has an active length of 2.30 m with its inner layer of 26 sense wires at a radius of 25.0 cm and its outer layer of 136 sense wires at a radius of 144.4 cm. A minimum double-track separation of 5 mm has so far been achieved, which is considerably better than in the old chamber which had no multihit capability in a cell.

For the test run at PEP, a cylindrical trigger drift chamber[22] is located between the main drift chamber and the beam pipe. The trigger drift chamber consists of six layers of axial sense wires in 4-mm-radius aluminized Mylar tubes. The inner layer of this chamber has 72 wires at a radius of 9.5 cm, and the outer layer has 112 wires at a radius of 14.8 cm. The sense wires in the

TABLE IV. The cuts for hadronic event selection.

Cut	Cut definition	PEP 5	Upgraded
1	At least five well-reconstructed charged tracks.	89%	91%
2	Sum of charged energy $\geq 27.5\%$ of $E_{c.m.}$.	67%	87%
3	Sum of charged track and photon energy $\geq 55\%$ of $E_{c.m.}$.	48%	70%
4	The z coordinate of the event vertex to be within 20 cm of the measured interaction point.	48%	70%
5	$\lvert\cos\theta_T\rvert < 0.55$ for the PEP 5 data set and $\lvert\cos\theta_T\rvert < 0.8$ for the upgraded data set with θ_T=angle between thrust axis and incoming beam.	38%	60%
6	$p_{miss} < E_{c.m.}/4$ with p_{miss}=magnitude of the missing-momentum vector.	35%	57%
7	For events with $p_{miss} > 2$ GeV/c, we demand $\lvert\cos\theta_{miss}\rvert < 0.9$ with θ_{miss}=angle between p_{miss} and incoming beam.	33%	52%
8	In 2-jet events, if both jets have fewer than five charged and neutral particles, then the invariant masses of both jets have to exceed 2 GeV/c.	33%	52%
9	Events, with an observed photon of $E_\gamma \geq 3$ GeV as well as $E_\gamma \geq 90\%$ of the observed energy of the jet to which it is assigned are removed.	32.5%	51%

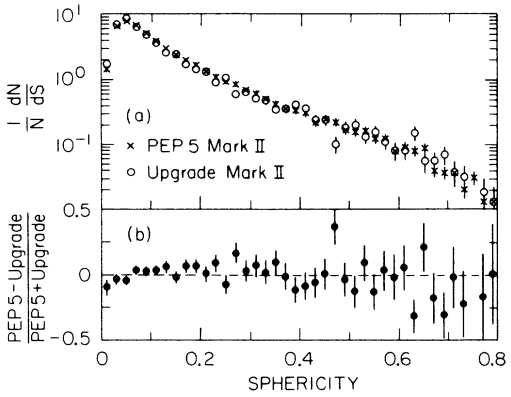

FIG. 3. Comparison of the corrected distributions from the PEP 5 Mark II detector and the upgraded one, (a) sphericity, (b) the ratio (upgrade − PEP 5)/(upgrade + PEP 5) for the sphericity distribution.

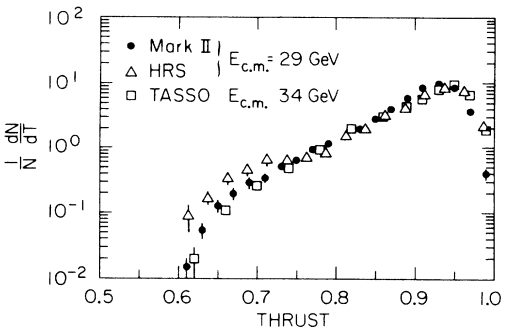

FIG. 5. Comparison of the thrust distribution with HRS and TASSO results.

main drift chamber have an average point measurement resolution of 175 μm, and the trigger drift chamber wires have one of 90 μm. Both the new trigger drift chamber and the new main drift chamber are used for charged-track reconstruction resulting in a measured momentum resolution of $(\delta p/p)^2 = 0.014^2 + (0.0026p)^2$.

The photon reconstruction is provided by the original central region lead–liquid-argon calorimeter modules but with a different amplifier gain and new end-cap electromagnetic calorimeters.[23] The end caps are sandwiches of proportional tubes separated by 0.5 radiation lengths of lead. In total, 36 layers of tubes are arranged along four different coordinates axes: x, y, u, and v. This results in 18 radiation lengths sampled by approximately 9000 proportional cells per end cap. The energy resolution measured with Bhabha pairs is $0.22/\sqrt{E}$ (E in GeV).

IV. PARTICLE AND EVENT SELECTION

The charged-track selection criteria are the following: a well-reconstructed track has to pass within 4 cm in radius (distance of closest approach perpendicular to the beam axis) and 6 cm in z from the event vertex and have at least 100 MeV/c of transverse momentum with respect to the incoming beams. The measured momentum is corrected for energy loss in the material in front of the tracking chambers assuming the particle to be a pion. Photons are detected by their electromagnetic showers in the calorimeters. A neutral cluster with energy greater than 150 MeV and a distance (at the radius of the shower counter) of more than 30 cm from the closest charged track is defined as a photon.

Hadronic events were selected by making the requirements given in Table IV. The two numbers at the end of each cut definition show the percentages of multihadronic events which pass that and all the above cuts, as estimated from Monte Carlo calculations. The first number corresponds to the original detector, the second to the upgrade. The increase in the $\cos\theta_T$ cut for the upgraded data is due to the better coverage of the central drift chamber and the new end caps.

For the jet definition, a cluster algorithm[6] which utilizes the vector momenta of charged and neutral particles and partitions the events into a number of reconstructed jets is used.

The cuts discriminate against poorly reconstructed events, beam-gas scattering (cuts 4, 6, 7), two photon

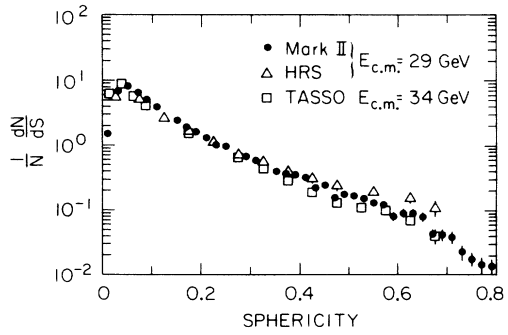

FIG. 4. Comparison of the sphericity distribution with HRS and TASSO results.

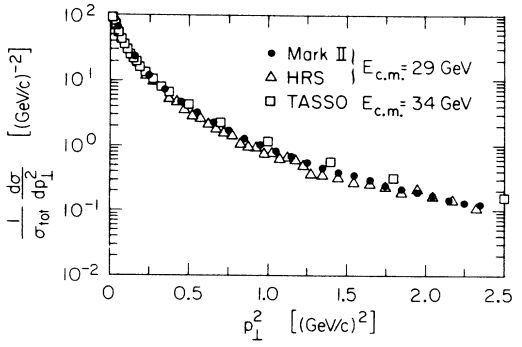

FIG. 6. Comparison of the $p_\perp^2$ distribution with HRS and TASSO results.

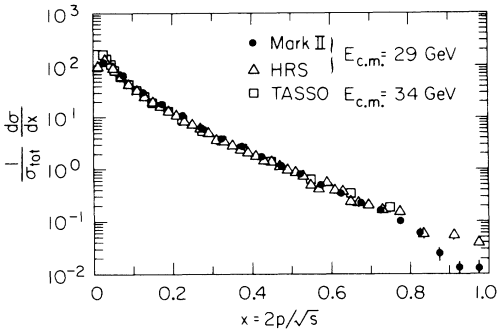

FIG. 7. Comparison of the inclusive particle x distribution with HRS and TASSO results.

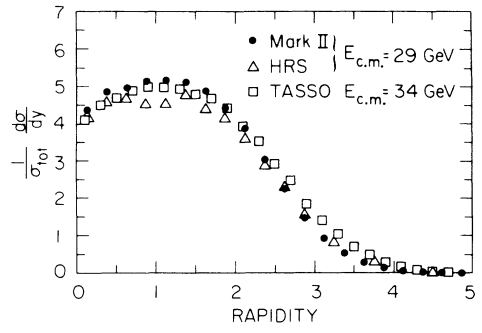

FIG. 8. Comparison of the rapidity distribution with HRS and TASSO results.

events (6,7), τ pair production (1,8) and events with initial- or final-state photon radiation (7,9). The contamination of the accepted events by these processes was found to be small: $<0.2\%$ from τ pair production, $<1.0\%$ from $\gamma\gamma$ scattering, and a negligible amount from beam-gas scattering.

A total of 22 000 events of PEP 5 data and 7400 events of upgraded data passed the selection criteria.

V. DEFINITION OF THE OBSERVABLES

The properties of the events are studied in both global event shape observables and inclusive particle distributions. All charged and neutral particles are used for calculating event shapes, axes, and jet masses.

The eigenvalues of the sphericity tensor[24] are taken to characterize the events according to their shape in momentum space. For each event the eigenvalues Q_1, Q_2, Q_3 ($Q_1<Q_2<Q_3$ and $Q_1+Q_2+Q_3=1$) and the corresponding principal axes $\mathbf{q}_1$, $\mathbf{q}_2$, $\mathbf{q}_3$ of the momentum ellipsoid are calculated. The sphericity axis ($\mathbf{q}_3$) is usually taken as the event axis and the event plane is defined by ($\mathbf{q}_2,\mathbf{q}_3$). In terms of the Q_i, the aplanarity is defined by $A=\frac{3}{2}Q_1$, the sphericity by $S=\frac{3}{2}(Q_1+Q_2)$ and the variable Q_x by $Q_x=(Q_3-Q_2)/\sqrt{3}$. Because of the fact that the sphericity tensor uses the momenta of the particles quadratically, those observables are more sensitive to the high-momentum particles in an event than observables which use momenta linearly.

TABLE V. The aplanarity distribution, $(1/N)dN/dA$.

Aplanarity	Data averaged	PEP 5 detector	Upgraded detector
0.00–0.01	15.0±0.57	14.8±0.57	15.4±0.69
0.01–0.02	28.0±0.83	27.6±0.83	28.6±1.04
0.02–0.03	20.2±0.77	20.5±0.79	19.8±0.91
0.03–0.04	12.4±0.50	12.5±0.52	12.2±0.62
0.04–0.05	7.76±0.33	8.02±0.35	7.38±0.43
0.05–0.06	5.11±0.23	5.14±0.25	5.06±0.33
0.06–0.07	3.51±0.26	3.50±0.28	3.51±0.33
0.07–0.08	2.48±0.19	2.53±0.21	2.40±0.25
0.08–0.09	1.59±0.17	1.53±0.18	1.69±0.23
0.09–0.10	1.13±0.13	1.09±0.14	1.18±0.17
0.10–0.11	0.800±0.092	0.758±0.099	0.888±0.141
0.11–0.12	0.506±0.061	0.527±0.072	0.471±0.093
0.12–0.13	0.442±0.055	0.403±0.058	0.572±0.105
0.13–0.14	0.298±0.040	0.267±0.042	0.435±0.088
0.14–0.15	0.214±0.031	0.222±0.036	0.196±0.054
0.15–0.16	0.182±0.028	0.172±0.030	0.219±0.058
0.16–0.17	0.155±0.025	0.149±0.027	0.177±0.051
0.17–0.18	0.114±0.020	0.104±0.021	0.171±0.050
0.18–0.19	0.088±0.017	0.086±0.019	0.096±0.036
0.19–0.20	0.071±0.015	0.071±0.016	0.070±0.029
0.20–0.21	0.051±0.012	0.054±0.014	0.043±0.022
0.21–0.22	0.018±0.006	0.023±0.009	0.010±0.010
0.22–0.23	0.017±0.010	0.033±0.010	0.001±0.010
0.23–0.24	0.024±0.008	0.023±0.009	0.029±0.017
$\langle A \rangle$	0.031±0.001	0.031±0.001	0.031±0.001

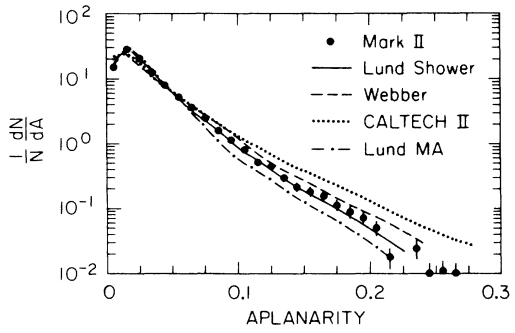

FIG. 9. The aplanarity distribution in comparison with the models.

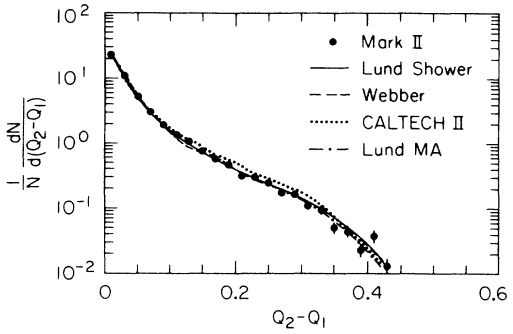

FIG. 11. The Q_2-Q_1 distribution in comparison with the models.

Another way of measuring the event structure is the thrust,[25] which is defined as $T=\max(\sum|p_{\|i}|/\sum|p_i|)$, where $p_{\|i}$ is the longitudinal momentum of particle i relative to the thrust axis, which is chosen such as to maximize $\sum|p_{\|i}|$. The axis with the greatest thrust value perpendicular to the thrust axis is defined to be the major axis, and the thrust along this axis is the major value.[26] The minor axis is defined to give an orthonormal system, and the minor value is again the sum of parallel momenta with respect to this axis over the sum of momenta. The oblateness is the difference of the major and minor values. Because these observables use momenta linearly, they are much more sensitive to the soft particle production than those from sphericity analysis, and past experience has shown that their distributions are more difficult to describe using the models.

A third measure of the hadronic final state with sound perturbative properties is the jet invariant mass proposed by Clavelli and Wyler[27] though we use a slightly different definition. The event is divided into two hemispheres by the plane perpendicular to the sphericity axis, and the invariant mass of all particles in each hemisphere is calculated. The smaller value defines $M_{\rm sl}$, the mass of the slim jet, and the other $M_{\rm br}$, the mass of the broad jet. The quantities of interest are $M_{\rm br}^2/s$, $M_{\rm sl}^2/s$, and $(M_{\rm br}^2-M_{\rm sl}^2)/s$ with $s=E_{\rm c.m.}^2$.

Measurements of the inclusive distributions of charged particles within hadronic events are given in $x=2p/E_{\rm c.m.}$, $p_\perp$, and $p_\perp^2$ (with respect to the sphericity axis), $p_\perp^{\rm in}$ and $p_\perp^{\rm out}$, the transverse momenta in and out of the event plane, the rapidity $y=\frac{1}{2}\ln[(E+p_\|)/(E-p_\|)]$, where is this case $p_\|$ is the component of momentum parallel to the thrust axis, and the charged particle flow $dn/d\theta$, where θ is the angle between the particle and the sphericity axis. Finally, the energy flow $dE/d\theta$ is used, which is equal to $dn/d\theta$ weighted by the energies of the charged and neutral particles.

VI. CORRECTIONS

To correct the observed distributions for acceptance inefficiencies, other detector imperfections, effects from radiated photons, and the above described cuts, Monte Carlo simulation programs are used. The production of multihadronic events was computed based on four different models for QCD plus fragmentation: the independent parton fragmentation model of Ali *et al.*,[28] and the Lund string fragmentation model, both of which employ parton emission to second order in α_s, and the QCD shower models of Webber and Lund, which use

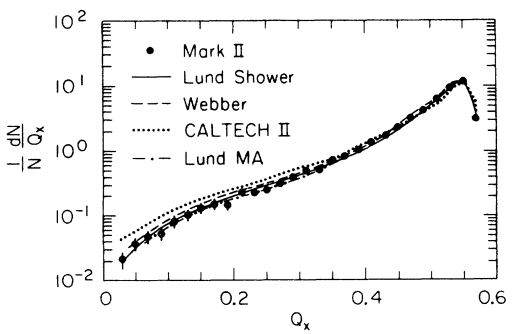

FIG. 10. The Q_x distribution in comparison with the models.

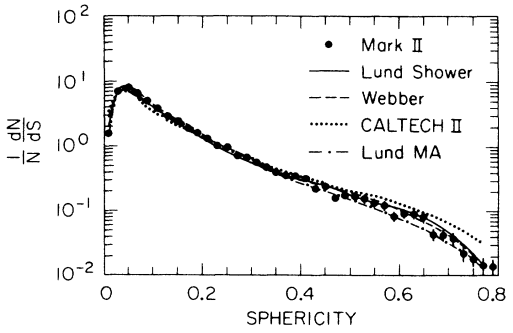

FIG. 12. The sphericity distribution in comparison with the models.

TABLE VI. The Q_x distribution, $(1/N)dN/dQ_x$.

Q_x	Data averaged	PEP 5 detector	Upgraded detector
0.00–0.02	0.007±0.003	0.007±0.003	0.006±0.006
0.02–0.04	0.021±0.006	0.021±0.006	0.022±0.012
0.04–0.06	0.037±0.008	0.051±0.012	0.022±0.012
0.06–0.08	0.048±0.011	0.053±0.012	0.040±0.017
0.08–0.10	0.053±0.012	0.049±0.011	0.069±0.023
0.10–0.12	0.082±0.017	0.075±0.016	0.110±0.032
0.12–0.14	0.104±0.020	0.115±0.023	0.088±0.027
0.14–0.16	0.134±0.026	0.129±0.025	0.148±0.039
0.16–0.18	0.152±0.028	0.141±0.027	0.180±0.045
0.18–0.20	0.147±0.027	0.201±0.037	0.109±0.031
0.20–0.22	0.233±0.031	0.217±0.030	0.282±0.052
0.22–0.24	0.232±0.030	0.257±0.034	0.197±0.041
0.24–0.26	0.256±0.032	0.283±0.037	0.219±0.044
0.26–0.28	0.321±0.039	0.321±0.041	0.322±0.057
0.28–0.30	0.410±0.041	0.418±0.044	0.396±0.061
0.30–0.32	0.507±0.049	0.475±0.049	0.587±0.079
0.32–0.34	0.515±0.045	0.515±0.048	0.516±0.069
0.34–0.36	0.740±0.061	0.761±0.067	0.705±0.085
0.36–0.38	0.872±0.054	0.916±0.062	0.792±0.083
0.38–0.40	1.08±0.07	1.08±0.07	1.10±0.10
0.40–0.42	1.42±0.08	1.41±0.09	1.44±0.12
0.42–0.44	1.72±0.08	1.74±0.09	1.69±0.13
0.44–0.46	2.39±0.11	2.47±0.12	2.26±0.15
0.46–0.48	3.24±0.14	3.26±0.15	3.21±0.20
0.48–0.50	4.37±0.19	4.52±0.20	4.14±0.24
0.50–0.52	6.32±0.26	6.48±0.27	6.10±0.31
0.52–0.54	9.67±0.37	9.91±0.38	9.35±0.44
0.54–0.56	11.9±0.46	11.5±0.45	12.5±0.57
0.56–0.58	3.21±0.16	3.11±0.16	3.40±0.21
$\langle Q_x \rangle$	0.490±0.01	0.489±0.01	0.491±0.01

leading-logarithmic evolution for the parton showering including soft-gluon interference.

As the first step, N_{gen} Monte Carlo events were generated at fixed $E_{c.m.}=29$ GeV without QED radiative effects. These events yield the distributions $n_{gen}(x)$ of all long-lived particles ($K^{\pm}$, K_L^0, $\pi^{\pm}$, $\mu^{\pm}$, $e^{\pm}$, γ, p, $\bar{p}$, n, $\bar{n}$, and ν) produced either at the primary vertices or from the decays of all short-lived particles such as K_S^0, strange baryons, resonances, and particles containing charm and bottom quarks. For distributions of quantities which depend on the particle masses the actual masses of the particles are used.

For the second step, events were generated including QED radiative effects[29] and traced through either the PEP 5 or the upgraded detector. Energy loss, multiple scattering, photon conversion, and nuclear interactions

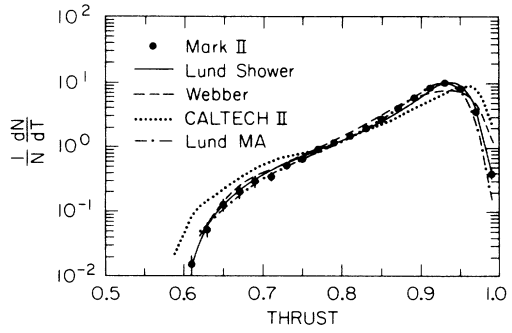

FIG. 13. The thrust distribution in comparison with the models.

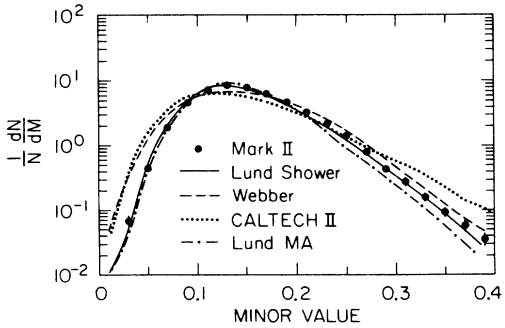

FIG. 14. The minor-value distribution in comparison with the models.

TABLE VII. The Q_2-Q_1 distribution, $(1/N)dN/d(Q_2-Q_1)$.

Q_2-Q_1	Data averaged	PEP 5 detector	Upgraded detector
0.00–0.02	23.0±0.70	22.9±0.85	23.1±0.99
0.02–0.04	11.0±0.46	11.0±0.47	10.9±0.52
0.04–0.06	5.31±0.23	5.45±0.25	5.14±0.28
0.06–0.08	3.16±0.20	3.18±0.22	3.12±0.24
0.08–0.10	1.97±0.11	2.01±0.12	1.91±0.15
0.10–0.12	1.37±0.09	1.39±0.10	1.35±0.13
0.12–0.14	1.07±0.08	1.02±0.09	1.16±0.12
0.14–0.16	0.76±0.06	0.79±0.07	0.72±0.09
0.16–0.18	0.571±0.049	0.551±0.051	0.619±0.078
0.18–0.20	0.460±0.045	0.464±0.048	0.452±0.066
0.20–0.22	0.313±0.038	0.338±0.043	0.277±0.051
0.22–0.24	0.298±0.036	0.310±0.040	0.277±0.051
0.24–0.26	0.244±0.031	0.241±0.032	0.252±0.048
0.26–0.28	0.174±0.023	0.171±0.024	0.180±0.039
0.28–0.30	0.167±0.022	0.164±0.024	0.174±0.038
0.30–0.32	0.112±0.016	0.120±0.018	0.097±0.027
0.32–0.34	0.094±0.014	0.087±0.015	0.123±0.031
0.34–0.36	0.050±0.009	0.048±0.010	0.058±0.020
0.36–0.38	0.045±0.008	0.059±0.011	0.026±0.013
0.38–0.40	0.023±0.005	0.029±0.007	0.013±0.009
0.40–0.42	0.037±0.008	0.037±0.008	0.039±0.016
0.42–0.44	0.013±0.004	0.013±0.004	0.013±0.009
0.44–0.46	0.008±0.003	0.007±0.003	0.013±0.009
$\langle Q_2-Q_1 \rangle$	0.045±0.001	0.045±0.001	0.044±0.001

in the material of the detector, as well as decays, were taken into account. This information was then converted into the measured quantities, such as drift times and pulse heights, taking the properties of the apparatus into account. The events were then passed through the same reconstruction algorithms and analysis programs used for the two samples of real data. The accepted events N_{det} produce the detector particle distributions $n_{\text{det}}(x)$.

The corrected distribution $dn_{\text{cor}}(x)$ as a function of a variable x is then obtained from the measured distribution $dn_{\text{meas}}(x)$ by using a bin-by-bin correction function $C(x)$ (Ref. 30):

$$dn_{\text{cor}}(x)=C(x)dn_{\text{meas}}(x) .$$

The values of $C(x)$ are calculated by

$$C(x)=\frac{n_{\text{gen}}(x)}{N_{\text{gen}}}\Big/\frac{n_{\text{det}}(x)}{N_{\text{det}}} .$$

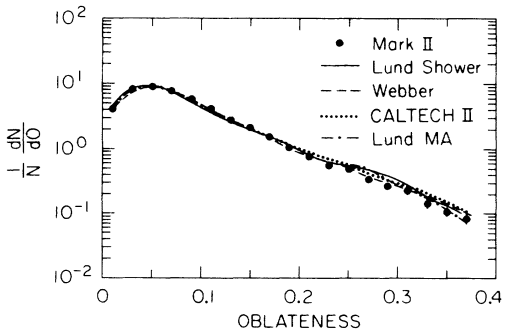

FIG. 15. The oblateness distribution in comparison with the models.

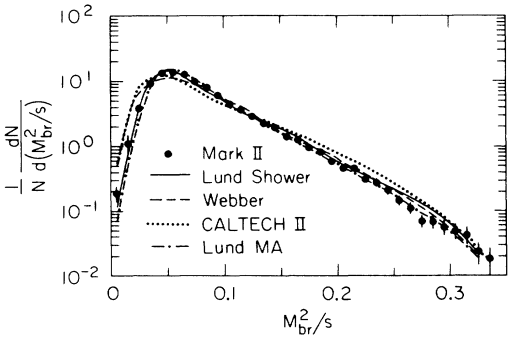

FIG. 16. The M_{br}^2/s distribution in comparison with the models.

TABLE VIII. The sphericity distribution, $(1/N)dN/dS$.

Sphericity	Data averaged	PEP 5 detector	Upgraded detector
0.00–0.02	1.54±0.10	1.43±0.11	1.75±0.15
0.02–0.04	6.79±0.34	6.62±0.33	7.06±0.42
0.04–0.06	8.09±0.32	7.83±0.31	8.53±0.40
0.06–0.08	6.54±0.25	6.71±0.26	6.28±0.32
0.08–0.10	4.99±0.20	5.09±0.21	4.82±0.26
0.10–0.12	3.81±0.16	3.92±0.17	3.65±0.21
0.12–0.14	2.90±0.15	3.06±0.17	2.69±0.19
0.14–0.16	2.44±0.14	2.41±0.14	2.49±0.18
0.16–0.18	1.90±0.11	2.01±0.12	1.75±0.14
0.18–0.20	1.61±0.09	1.69±0.10	1.47±0.13
0.20–0.22	1.34±0.09	1.34±0.10	1.32±0.13
0.22–0.24	1.03±0.07	1.11±0.08	0.92±0.10
0.24–0.26	0.982±0.080	0.935±0.079	1.084±0.116
0.26–0.28	0.738±0.061	0.857±0.073	0.607±0.077
0.28–0.30	0.680±0.057	0.696±0.061	0.652±0.081
0.30–0.32	0.581±0.055	0.618±0.062	0.529±0.073
0.32–0.34	0.504±0.049	0.515±0.053	0.484±0.069
0.34–0.36	0.403±0.040	0.435±0.046	0.355±0.056
0.36–0.38	0.365±0.040	0.364±0.043	0.368±0.060
0.38–0.40	0.358±0.040	0.336±0.040	0.420±0.066
0.40–0.42	0.329±0.040	0.312±0.040	0.368±0.062
0.42–0.44	0.227±0.029	0.220±0.030	0.245±0.047
0.44–0.46	0.249±0.031	0.251±0.033	0.245±0.047
0.46–0.48	0.160±0.021	0.227±0.031	0.104±0.028
0.48–0.50	0.179±0.024	0.176±0.025	0.187±0.040
0.50–0.52	0.171±0.023	0.160±0.023	0.206±0.042
0.52–0.54	0.155±0.021	0.166±0.024	0.136±0.033
0.54–0.56	0.133±0.019	0.125±0.019	0.161±0.037
0.56–0.58	0.122±0.017	0.125±0.019	0.116±0.030
0.58–0.60	0.082±0.013	0.081±0.014	0.084±0.025
0.60–0.62	0.091±0.014	0.094±0.015	0.084±0.025
0.62–0.64	0.091±0.014	0.081±0.014	0.155±0.036
0.64–0.66	0.079±0.012	0.090±0.015	0.058±0.020
0.66–0.68	0.043±0.008	0.041±0.009	0.058±0.020
0.68–0.70	0.042±0.008	0.038±0.008	0.071±0.023
0.70–0.72	0.038±0.008	0.038±0.008	0.039±0.016
0.72–0.74	0.022±0.005	0.021±0.006	0.032±0.015
0.74–0.76	0.018±0.004	0.031±0.007	0.007±0.006
0.76–0.78	0.014±0.004	0.013±0.005	0.019±0.011
0.78–0.80	0.013±0.004	0.013±0.005	0.013±0.009
$\langle S \rangle$	0.129±0.004	0.130±0.004	0.128±0.004

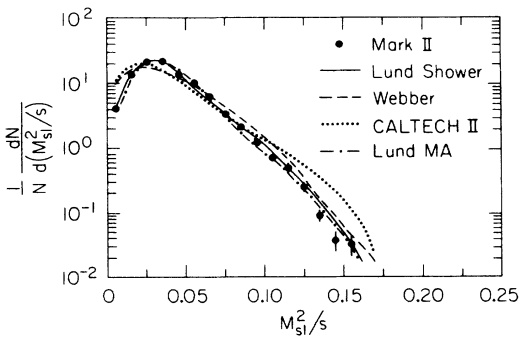

FIG. 17. The M_{sl}^2/s distribution in comparison with the models.

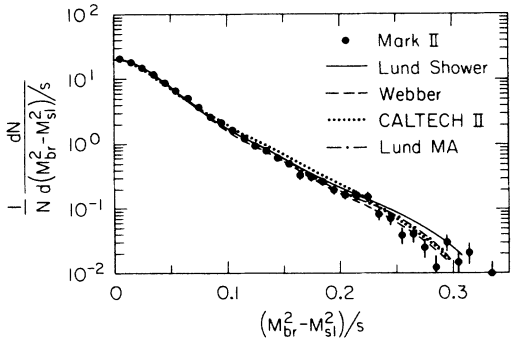

FIG. 18. The $(M_{br}^2-M_{sl}^2)/s$ distribution in comparison with the models.

TABLE IX. The thrust distribution, $(1/N)dN/dT$.

Thrust	Data averaged	PEP 5 Detector	Upgraded detector
0.56–0.58	0.001±0.001	0.002±0.002	0.001±0.001
0.58–0.60	0.001±0.001	0.003±0.002	0.001±0.001
0.60–0.62	0.015±0.005	0.013±0.005	0.027±0.015
0.62–0.64	0.053±0.013	0.050±0.013	0.061±0.024
0.64–0.66	0.125±0.027	0.113±0.025	0.183±0.054
0.66–0.68	0.195±0.039	0.222±0.045	0.163±0.049
0.68–0.70	0.286±0.055	0.301±0.059	0.265±0.068
0.70–0.72	0.344±0.052	0.375±0.058	0.305±0.064
0.72–0.74	0.514±0.063	0.555±0.069	0.461±0.078
0.74–0.76	0.646±0.067	0.667±0.071	0.615±0.089
0.76–0.78	0.930±0.095	0.947±0.098	0.905±0.12
0.78–0.80	1.15±0.09	1.14±0.09	1.15±0.12
0.80–0.82	1.45±0.08	1.46±0.09	1.43±0.12
0.82–0.84	1.92±0.11	2.03±0.12	1.76±0.14
0.84–0.86	2.67±0.12	2.65±0.12	2.72±0.17
0.86–0.88	3.91±0.16	4.28±0.18	3.43±0.20
0.88–0.90	5.83±0.22	6.21±0.24	5.33±0.28
0.90–0.92	8.19±0.24	8.36±0.25	7.91±0.32
0.92–0.94	9.88±0.36	9.67±0.39	10.16±0.45
0.94–0.96	8.17±0.38	7.69±0.36	8.91±0.45
0.96–0.98	3.56±0.29	3.45±0.28	3.72±0.35
0.98–1.00	0.39±0.07	0.35±0.06	0.51±0.11
$\langle 1-T \rangle$	0.103±0.004	0.105±0.004	0.101±0.004

For most of the distributions $C(x)$ varies between 0.7 and 1.4 with the values being closer to unity for the upgraded detector than for the PEP 5 detector. The correction factors for each of the two samples are averaged between the results of the different models, but a higher weight is given to those models which describe the uncorrected data best. The differences between the averaged value and those of the different models are taken as measures of the systematic uncertainty in the corrections. The errors shown for the corrected distributions contain the quadratic sum of the statistical error of the data and the systematic error in the correction.

TABLE X. The minor-value distribution, $(1/N)dN/dM$.

Minor	Data averaged	PEP 5 detector	Upgraded detector
0.00–0.02	0.009±0.003	0.008±0.003	0.012±0.006
0.02–0.04	0.067±0.013	0.074±0.014	0.057±0.018
0.04–0.06	0.444±0.048	0.416±0.046	0.508±0.071
0.06–0.08	1.86±0.13	1.80±0.13	1.95±0.17
0.08–0.10	4.53±0.21	4.35±0.20	4.89±0.28
0.10–0.12	7.26±0.23	7.19±0.24	7.40±0.32
0.12–0.14	8.42±0.26	8.25±0.26	8.72±0.35
0.14–0.16	7.96±0.24	8.07±0.25	7.77±0.32
0.16–0.18	6.38±0.20	6.67±0.21	5.93±0.27
0.18–0.20	4.63±0.15	4.83±0.16	4.29±0.21
0.20–0.22	3.25±0.14	3.37±0.15	3.05±0.19
0.22–0.24	2.20±0.10	2.30±0.11	2.03±0.14
0.24–0.26	1.39±0.08	1.39±0.08	1.39±0.12
0.26–0.28	0.801±0.064	0.829±0.069	0.753±0.089
0.28–0.30	0.437±0.047	0.453±0.050	0.409±0.065
0.30–0.32	0.279±0.034	0.279±0.036	0.277±0.052
0.32–0.34	0.159±0.022	0.160±0.023	0.156±0.035
0.34–0.36	0.091±0.014	0.095±0.015	0.081±0.024
0.36–0.38	0.057±0.010	0.059±0.011	0.052±0.018
0.38–0.40	0.035±0.007	0.038±0.008	0.029±0.013
$\langle M \rangle$	0.153±0.005	0.154±0.005	0.151±0.005

TABLE XI. The oblateness distribution, $(1/N)dN/dO$.

Oblateness	Data averaged	PEP 5 detector	Upgraded detector
0.00–0.02	4.05±0.25	3.90±0.25	4.31±0.32
0.02–0.04	8.26±0.45	7.98±0.44	8.67±0.53
0.04–0.06	9.02±0.35	9.10±0.35	8.91±0.42
0.06–0.08	7.70±0.24	7.75±0.25	7.60±0.32
0.08–0.10	5.88±0.20	5.96±0.21	5.76±0.27
0.10–0.12	4.23±0.24	4.34±0.25	4.09±0.27
0.12–0.14	2.81±0.23	2.94±0.24	2.68±0.24
0.14–0.16	2.17±0.13	2.19±0.14	2.13±0.17
0.16–0.18	1.56±0.10	1.56±0.10	1.55±0.13
0.18–0.20	1.07±0.08	1.12±0.09	1.01±0.10
0.20–0.22	0.773±0.071	0.886±0.083	0.660±0.083
0.22–0.24	0.559±0.061	0.609±0.067	0.501±0.072
0.24–0.26	0.501±0.055	0.487±0.055	0.527±0.075
0.26–0.28	0.347±0.039	0.410±0.047	0.281±0.048
0.28–0.30	0.268±0.034	0.309±0.040	0.222±0.043
0.30–0.32	0.230±0.033	0.234±0.034	0.224±0.045
0.32–0.34	0.144±0.022	0.150±0.023	0.133±0.031
0.34–0.36	0.106±0.016	0.147±0.023	0.071±0.021
0.36–0.38	0.084±0.014	0.079±0.014	0.102±0.027
0.38–0.40	0.162±0.024	0.192±0.029	0.128±0.031
$\langle O \rangle$	0.086±0.004	0.087±0.004	0.083±0.004

VII. COMPARISON OF DATA FROM THE PEP 5 AND THE UPGRADED DETECTOR

Despite the differences in the instrumentation of the PEP 5 and upgraded detectors, the corrected distributions of the two sets of data taken agree remarkably well. The χ^2/DF scatter is close to unity for all corrected distributions. The largest deviation is visible in the thrust distribution [Fig. 2(a)] with a χ^2/DF of 1.5. The ratio (PEP 5 detector − upgraded detector)/(PEP 5 detector + upgraded detector) for the thrust distribution, shown in Fig. 2(b), does not indicate any obvious systematic shift. As an example of the typical agreement between the two data sets we show the distributions for the sphericity in Figs. 3(a) and 3(b). Taking a close look at the comparison, the upgraded data might indicate slightly slimmer event shapes. The average $p_\perp$ ($p_\perp^2$) (see Tables XVI and XV) are 5 MeV/c [5 (MeV/c)^2] smaller and the average sphericity (see Table VIII) is 1.5% smaller for the upgrade than for the PEP 5 data, but these deviations lie within the quoted errors. The integrals over the different inclusive charged-particle distributions (such as x, rapidity, $p_\perp$, and particle flow), which give the average charged multiplicity, vary between 12.84 and 12.96. For the two samples, the resulting multiplicity is on the average 0.05 higher for the new data than for the old, but this difference is smaller than the resulting errors.

Because of the good agreement between the two sets of data, we have combined them into one set by averaging the two values weighted by their errors. The new total error is calculated as the inverse quadratic sum of the statistical errors of the two data sets, and the systematic

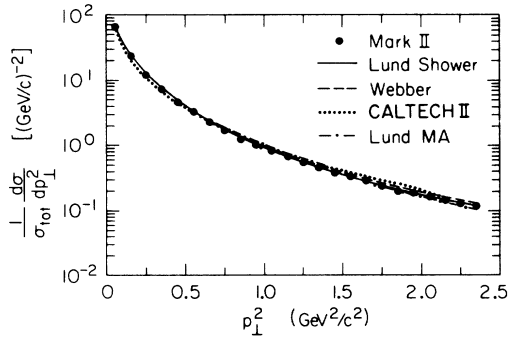

FIG. 19. The $p_\perp^2$ distribution of charged particles with respect to the sphericity axis in comparison with the models.

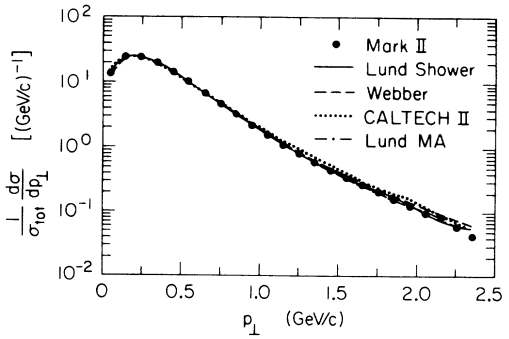

FIG. 20. The $p_\perp$ distribution of charged particles with respect to the sphericity axis in comparison with the models.

TABLE XII. The invariant mass squared of the broad jet, $(1/N)dN/d(M_{\rm br}^2/s)$.

$M_{\rm br}^2/s$	Data averaged	PEP 5 detector	Upgraded detector
0.00–0.01	0.19±0.05	0.15±0.06	0.26±0.09
0.01–0.02	1.13±0.32	1.13±0.32	1.14±0.46
0.02–0.03	3.93±0.57	3.89±0.56	3.99±0.62
0.03–0.04	8.95±0.71	7.56±0.74	11.2±0.93
0.04–0.05	13.1±0.77	12.1±0.83	14.3±0.93
0.05–0.06	13.4±0.59	13.2±0.87	13.6±0.92
0.06–0.07	12.4±0.62	13.1±0.86	11.7±0.87
0.07–0.08	9.93±0.58	10.7±0.67	9.10±0.70
0.08–0.09	7.86±0.48	8.55±0.53	7.04±0.57
0.09–0.10	6.11±0.43	6.38±0.50	5.76±0.57
0.10–0.11	4.42±0.35	4.68±0.39	4.11±0.43
0.11–0.12	3.65±0.31	3.92±0.34	3.33±0.36
0.12–0.13	2.93±0.26	2.90±0.26	2.97±0.33
0.13–0.14	2.25±0.20	2.33±0.22	2.14±0.26
0.14–0.15	1.95±0.18	1.99±0.19	1.89±0.24
0.15–0.16	1.42±0.14	1.46±0.14	1.37±0.19
0.16–0.17	1.29±0.12	1.28±0.13	1.30±0.18
0.17–0.18	0.964±0.096	0.939±0.10	1.027±0.16
0.18–0.19	0.819±0.084	0.821±0.087	0.815±0.13
0.19–0.20	0.592±0.065	0.595±0.069	0.587±0.11
0.20–0.21	0.464±0.053	0.455±0.056	0.490±0.10
0.21–0.22	0.469±0.053	0.519±0.061	0.374±0.084
0.22–0.23	0.314±0.040	0.307±0.042	0.342±0.080
0.23–0.24	0.280±0.037	0.281±0.039	0.277±0.071
0.24–0.25	0.209±0.030	0.229±0.035	0.163±0.053
0.25–0.26	0.145±0.024	0.157±0.028	0.114±0.044
0.26–0.27	0.112±0.021	0.112±0.023	0.114±0.044
0.27–0.28	0.069±0.014	0.060±0.016	0.196±0.059
0.28–0.29	0.068±0.015	0.076±0.018	0.049±0.028
0.29–0.30	0.056±0.014	0.052±0.015	0.082±0.037
0.30–0.31	0.049±0.013	0.057±0.015	0.032±0.023
0.31–0.32	0.043±0.012	0.041±0.013	0.049±0.028
0.32–0.33	0.023±0.009	0.026±0.010	0.017±0.016
0.33–0.34	0.018±0.008	0.019±0.009	0.017±0.016
$\langle M_{\rm br}^2/s \rangle$	0.078±0.003	0.080±0.003	0.077±0.003

TABLE XIII. The invariant mass squared of the slim jet, $(1/N)dN/d(M_{\rm sl}^2/s)$.

$M_{\rm sl}^2/s$	Data averaged	PEP 5 detector	Upgraded detector
0.00–0.01	4.17±0.63	3.95±0.77	4.41±0.81
0.01–0.02	14.1±1.3	14.9±1.5	13.3±1.5
0.02–0.03	21.6±1.2	20.7±1.4	22.6±1.5
0.03–0.04	21.6±1.1	21.2±1.2	22.0±1.3
0.04–0.05	13.7±0.83	13.8±0.9	13.6±1.0
0.05–0.06	10.2±0.61	11.2±0.7	9.03±0.74
0.06–0.07	6.23±0.37	6.72±0.41	5.54±0.51
0.07–0.08	3.38±0.29	3.63±0.32	3.02±0.38
0.08–0.09	2.16±0.20	2.28±0.21	1.95±0.28
0.09–0.10	1.25±0.12	1.27±0.13	1.19±0.20
0.10–0.11	0.724±0.095	0.775±0.11	0.632±0.14
0.11–0.12	0.507±0.071	0.517±0.077	0.482±0.12
0.12–0.13	0.254±0.043	0.270±0.048	0.218±0.072
0.13–0.14	0.091±0.018	0.182±0.038	0.039±0.028
0.14–0.15	0.038±0.012	0.053±0.018	0.020±0.020
0.15–0.16	0.033±0.012	0.042±0.016	0.020±0.019
$\langle M_{\rm sl}^2/s \rangle$	0.039±0.002	0.039±0.002	0.038±0.002

TABLE XIV. The mass-squared difference of the broad and slim jet, $(1/N)dN/d[(M_{br}^2-M_{sl}^2)/s]$.

$(M_{br}^2-M_{sl}^2)/s$	Data averaged	PEP 5 detector	Upgraded detector
0.00–0.01	19.9±0.46	19.3±0.47	21.2±0.69
0.01–0.02	17.7±0.41	17.2±0.42	18.9±0.63
0.02–0.03	14.4±0.46	14.7±0.48	13.9±0.60
0.03–0.04	11.6±0.37	11.8±0.39	11.2±0.51
0.04–0.05	8.65±0.29	8.97±0.30	8.06±0.41
0.05–0.06	6.45±0.28	6.79±0.30	5.92±0.37
0.06–0.07	5.00±0.31	4.95±0.31	5.07±0.40
0.07–0.08	3.64±0.26	3.85±0.28	3.37±0.32
0.08–0.09	2.61±0.20	2.78±0.21	2.39±0.25
0.09–0.10	2.17±0.17	2.27±0.18	2.02±0.22
0.10–0.11	1.66±0.15	1.65±0.15	1.67±0.20
0.11–0.12	1.23±0.12	1.20±0.13	1.29±0.18
0.12–0.13	0.964±0.099	0.949±0.11	0.992±0.15
0.13–0.14	0.811±0.092	0.867±0.11	0.734±0.12
0.14–0.15	0.634±0.074	0.596±0.077	0.734±0.12
0.15–0.16	0.516±0.062	0.499±0.066	0.557±0.10
0.16–0.17	0.338±0.043	0.369±0.052	0.285±0.069
0.17–0.18	0.320±0.042	0.310±0.045	0.353±0.078
0.18–0.19	0.273±0.037	0.279±0.041	0.258±0.065
0.19–0.20	0.197±0.029	0.191±0.031	0.217±0.058
0.20–0.21	0.168±0.024	0.241±0.037	0.095±0.037
0.21–0.22	0.166±0.026	0.160±0.027	0.190±0.054
0.22–0.23	0.154±0.024	0.144±0.025	0.204±0.056
0.23–0.24	0.083±0.016	0.097±0.019	0.054±0.028
0.24–0.25	0.070±0.014	0.063±0.015	0.136±0.045
0.25–0.26	0.038±0.010	0.034±0.011	0.082±0.034
0.26–0.27	0.040±0.010	0.046±0.013	0.027±0.019
0.27–0.28	0.025±0.008	0.022±0.008	0.041±0.024
0.28–0.29	0.012±0.006	0.012±0.006	0.000±0.000
0.29–0.30	0.030±0.008	0.043±0.012	0.014±0.014
0.30–0.31	0.014±0.006	0.014±0.007	0.014±0.014
0.31–0.32	0.021±0.007	0.020±0.008	0.027±0.019
0.32–0.33	0.006±0.003	0.005±0.004	0.027±0.019
0.33–0.34	0.010±0.005	0.009±0.005	0.014±0.014
$\langle(M_{br}^2-M_{sl}^2)/s\rangle$	0.040±0.002	0.040±0.002	0.040±0.002

error from the correction factors is added quadratically.

Tables V–XXII contain the averaged data values along with those from the PEP 5 and upgraded detectors separately. In the discussions which follow, we will always use the averaged data sets.

Comparisons of these data with results from TASSO[31] and HRS[32] Collaborations are given in Figs. 4–8 for the sphericity, thrust, $p_\perp^2$, particle x, and rapidity. The agreement with the TASSO results is fairly good, taking into account that their data are taken at $E_{c.m.}=34$ GeV. The differences between the distributions are in the

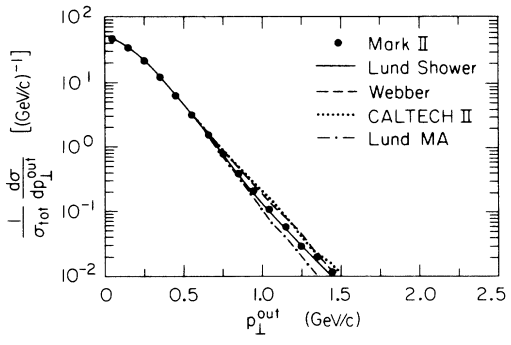

FIG. 21. The $p_\perp^{out}$ distribution of charged particles with respect to the event plane in comparison with the models.

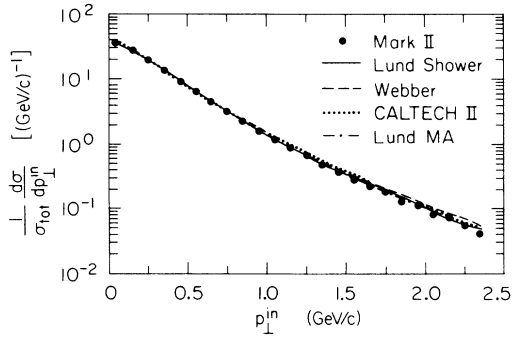

FIG. 22. The $p_\perp^{in}$ distribution of charged particles with respect to the sphericity axis in the event plane in comparison with the models.

TABLE XV. The transverse-momentum-squared distribution with respect to the sphericity axis, $(1/\sigma_{\text{tot}})d\sigma/dp_{\perp}^{2}$ [(GeV/c)$^{-2}$].

$p_{\perp}^{2}$ [(GeV/c)^2]	Data averaged	PEP 5 detector	Upgraded detector
0.0–0.1	65.4±0.55	65.3±0.56	65.5±0.67
0.1–0.2	23.3±0.23	23.3±0.23	23.4±0.29
0.2–0.3	12.0±0.23	11.7±0.23	12.3±0.26
0.3–0.4	7.26±0.14	7.28±0.15	7.23±0.17
0.4–0.5	4.71±0.14	4.72±0.14	4.69±0.16
0.5–0.6	3.29±0.10	3.25±0.10	3.33±0.12
0.6–0.7	2.31±0.071	2.36±0.07	2.25±0.09
0.7–0.8	1.71±0.069	1.69±0.07	1.74±0.08
0.8–0.9	1.29±0.053	1.29±0.054	1.28±0.064
0.9–1.0	1.03±0.043	1.05±0.045	1.00±0.053
1.0–1.1	0.825±0.042	0.857±0.045	0.786±0.050
1.1–1.2	0.671±0.035	0.691±0.037	0.644±0.043
1.2–1.3	0.548±0.029	0.557±0.031	0.534±0.037
1.3–1.4	0.454±0.024	0.501±0.028	0.400±0.030
1.4–1.5	0.381±0.024	0.396±0.026	0.360±0.030
1.5–1.6	0.342±0.024	0.371±0.028	0.309±0.029
1.6–1.7	0.292±0.024	0.292±0.025	0.293±0.030
1.7–1.8	0.241±0.022	0.244±0.023	0.236±0.027
1.8–1.9	0.208±0.019	0.190±0.019	0.248±0.028
1.9–2.0	0.189±0.017	0.189±0.019	0.188±0.023
2.0–2.1	0.166±0.015	0.177±0.017	0.152±0.020
2.1–2.2	0.144±0.014	0.154±0.016	0.131±0.018
2.2–2.3	0.128±0.012	0.122±0.013	0.140±0.018
2.3–2.4	0.121±0.012	0.127±0.013	0.111±0.016
2.4–40	1.433±0.117	1.470±0.126	1.399±0.122
$\langle p_{\perp}^{2} \rangle$ [(GeV/c)^2]	0.255±0.007	0.258±0.007	0.253±0.007

TABLE XVI. The transverse-momentum distribution with respect to the sphericity axis, $(1/\sigma_{\text{tot}})d\sigma/dp_{\perp}$ [(GeV/c)$^{-1}$].

$p_{\perp}$ (GeV/c)	Data averaged	PEP 5 detector	Upgraded detector
0.0–0.1	13.3±0.19	13.4±0.20	13.3±0.26
0.1–0.2	24.5±0.41	24.6±0.41	24.4±0.48
0.2–0.3	24.3±0.43	24.2±0.43	24.5±0.50
0.3–0.4	19.6±0.35	19.3±0.35	19.8±0.41
0.4–0.5	14.2±0.26	14.0±0.26	14.4±0.31
0.5–0.6	9.90±0.28	9.93±0.28	9.85±0.31
0.6–0.7	6.76±0.19	6.84±0.20	6.66±0.21
0.7–0.8	4.69±0.14	4.75±0.14	4.61±0.16
0.8–0.9	3.14±0.094	3.16±0.10	3.12±0.11
0.9–1.0	2.14±0.066	2.19±0.07	2.08±0.08
1.0–1.1	1.52±0.062	1.59±0.066	1.45±0.07
1.1–1.2	1.07±0.045	1.15±0.050	0.980±0.053
1.2–1.3	0.808±0.035	0.835±0.038	0.771±0.044
1.3–1.4	0.576±0.026	0.564±0.027	0.599±0.037
1.4–1.5	0.431±0.024	0.451±0.026	0.402±0.031
1.5–1.6	0.329±0.019	0.349±0.021	0.301±0.025
1.6–1.7	0.262±0.020	0.253±0.020	0.279±0.027
1.7–1.8	0.202±0.015	0.195±0.016	0.216±0.023
1.8–1.9	0.154±0.015	0.163±0.017	0.143±0.019
1.9–2.0	0.122±0.013	0.130±0.015	0.112±0.017
2.0–2.1	0.093±0.010	0.088±0.011	0.106±0.016
2.1–2.2	0.081±0.009	0.076±0.010	0.090±0.014
2.2–2.3	0.058±0.007	0.063±0.008	0.050±0.010
2.3–2.4	0.042±0.005	0.048±0.007	0.033±0.008
2.4–10	0.216±0.021	0.222±0.024	0.208±0.026
$\langle p_{\perp} \rangle$ (GeV/c)	0.392±0.004	0.394±0.004	0.389±0.004

TABLE XVII. The momentum distribution out of the event plane, $(1/\sigma_{tot})d\sigma/dp_{\perp}^{out}$ [(GeV/c)$^{-1}$].

$p_{\perp}^{out}$ (GeV/c)	Data averaged	PEP 5 detector	Upgraded detector
0.0–0.1	47.2±0.81	46.8±0.80	47.8±0.92
0.1–0.2	34.5±0.61	34.1±0.61	35.0±0.69
0.2–0.3	21.8±0.39	21.7±0.39	21.9±0.44
0.3–0.4	12.4±0.22	12.5±0.23	12.3±0.26
0.4–0.5	6.45±0.12	6.48±0.12	6.41±0.15
0.5–0.6	3.24±0.09	3.32±0.092	3.14±0.11
0.6–0.7	1.59±0.058	1.61±0.061	1.55±0.073
0.7–0.8	0.790±0.037	0.807±0.039	0.765±0.048
0.8–0.9	0.397±0.020	0.392±0.022	0.406±0.031
0.9–1.0	0.212±0.015	0.219±0.016	0.200±0.021
1.0–1.1	0.107±0.011	0.109±0.012	0.104±0.016
1.1–1.2	0.058±0.008	0.060±0.009	0.054±0.012
1.2–1.3	0.030±0.005	0.032±0.006	0.026±0.007
1.3–1.4	0.020±0.004	0.020±0.004	0.020±0.006
1.4–1.5	0.012±0.003	0.012±0.003	0.010±0.004
1.5–1.6	0.006±0.002	0.008±0.002	0.004±0.002
$\langle p_{\perp}^{out} \rangle$ (GeV/c)	0.190±0.006	0.191±0.006	0.188±0.006

direction predicted by the models for such an energy difference. There are some deviations between our data and the HRS results.[32] The differences at very high thrust and low sphericity might result from somewhat higher background contamination, since they make less stringent cuts. For the $p_{\perp}^2$ distribution in Fig. 6, one has to take into account that HRS and TASSO calculate the $p_{\perp}$ relative to the thrust axis rather than to the sphericity axis.

VIII. COMPARISON OF THE DATA WITH THE MODELS

The averaged distributions of the data are shown in Figs. 9–26 and compared with the predictions of the Lund MA, Lund shower, CALTECH II, and Webber models.

The Lund MA model underestimates the tails of the aplanarity (Fig. 9), the minor value (Fig. 14), and the

TABLE XVIII. The transverse-momentum distribution in the event plane with respect to the sphericity axis, $(1/\sigma_{tot})d\sigma/dp_{\perp}^{in}$ [(GeV/c)$^{-1}$].

$p_{\perp}^{in}$ (GeV/c)	Data averaged	PEP 5 detector	Upgraded detector
0.0–0.1	35.8±0.56	36.0±0.56	35.7±0.67
0.1–0.2	27.5±0.47	27.5±0.47	27.5±0.55
0.2–0.3	19.5±0.35	19.2±0.35	19.8±0.41
0.3–0.4	13.4±0.25	13.3±0.25	13.5±0.29
0.4–0.5	9.39±0.18	9.27±0.18	9.57±0.22
0.5–0.6	6.53±0.13	6.47±0.13	6.60±0.16
0.6–0.7	4.42±0.093	4.42±0.10	4.43±0.12
0.7–0.8	3.24±0.098	3.21±0.10	3.27±0.12
0.8–0.9	2.27±0.071	2.27±0.073	2.27±0.086
0.9–1.0	1.59±0.065	1.61±0.068	1.57±0.076
1.0–1.1	1.18±0.049	1.23±0.053	1.13±0.058
1.1–1.2	0.87±0.037	0.905±0.041	0.823±0.046
1.2–1.3	0.67±0.029	0.673±0.032	0.665±0.040
1.3–1.4	0.477±0.022	0.460±0.023	0.512±0.033
1.4–1.5	0.365±0.020	0.375±0.023	0.351±0.028
1.5–1.6	0.284±0.018	0.290±0.021	0.276±0.025
1.6–1.7	0.221±0.017	0.217±0.018	0.228±0.024
1.7–1.8	0.186±0.016	0.183±0.017	0.190±0.022
1.8–1.9	0.129±0.013	0.136±0.015	0.120±0.017
1.9–2.0	0.113±0.012	0.115±0.014	0.110±0.016
2.0–2.1	0.081±0.009	0.079±0.010	0.086±0.014
2.1–2.2	0.072±0.008	0.068±0.009	0.082±0.013
2.2–2.3	0.054±0.007	0.058±0.008	0.049±0.010
2.3–2.4	0.041±0.005	0.044±0.006	0.037±0.008
2.4–10	0.201±0.020	0.210±0.023	0.191±0.024
$\langle p_{\perp}^{in} \rangle$ (GeV/c)	0.302±0.008	0.304±0.008	0.299±0.008

TABLE XIX. The scaled momentum distribution, $(1/\sigma_{\text{tot}})d\sigma/dx_p$, with $x_p = 2p/\sqrt{s}$.

x_p	Data averaged	PEP 5 detector	Upgraded detector
0.00–0.05	115.4±1.84	116.2±1.87	114.4±2.08
0.05–0.10	65.1±1.16	64.9±1.17	65.4±1.31
0.10–0.15	31.6±0.58	31.2±0.59	32.0±0.68
0.15–0.20	17.5±0.34	17.3±0.34	17.7±0.41
0.20–0.25	10.4±0.21	10.3±0.21	10.6±0.27
0.25–0.30	6.29±0.13	6.20±0.14	6.47±0.19
0.30–0.35	4.07±0.093	4.04±0.097	4.14±0.14
0.35–0.40	2.76±0.068	2.71±0.072	2.86±0.11
0.40–0.45	1.80±0.063	1.79±0.066	1.82±0.089
0.45–0.50	1.18±0.044	1.16±0.047	1.22±0.068
0.50–0.55	0.810±0.039	0.782±0.040	0.872±0.060
0.55–0.60	0.515±0.031	0.535±0.034	0.484±0.044
0.60–0.65	0.347±0.023	0.348±0.025	0.345±0.035
0.65–0.70	0.227±0.020	0.244±0.022	0.201±0.027
0.70–0.75	0.167±0.020	0.161±0.021	0.179±0.028
0.75–0.80	0.104±0.016	0.096±0.016	0.120±0.024
0.80–0.85	0.062±0.013	0.074±0.016	0.052±0.014
0.85–0.90	0.025±0.007	0.027±0.009	0.023±0.009
0.90–0.95	0.013±0.005	0.019±0.009	0.010±0.006
0.95–1.00	0.012±0.006	0.028±0.014	0.010±0.006
$\langle x_p \rangle$	0.092±0.004	0.092±0.004	0.093±0.004

$p_\perp^{\text{out}}$ distributions (Fig. 21). These indicate that the number of four and higher parton events is not well accounted for. The inclusive particle distribution in x (Fig. 23) is slightly overestimated in the region $0.3 < x < 0.7$. The thrust distribution (Fig. 13), which is often difficult to describe, is well described by this model. The study showed that the $(M_{\text{br}}^2 - M_{\text{sl}}^2)/s$ distribution (Fig. 18) is quite sensitive to the value of the scale parameter Λ and relatively insensitive to other parameters, including whether string or independent fragmentation is used. All the other distributions are fairly well described. For 50 000 simulated events the sum of χ^2 of all distributions is 1230 using 450 data points.

The CALTECH II model describes the data less well. It has a sum of χ^2 of 6830 for the same comparison. The number of events with high aplanarity is overestimated. For the sphericity, thrust, minor value, M_{br}^2/s, and M_{sl}^2/s distributions (Figs. 12–14, 16, and 17) it produces too many events with very low values, too few with medium values around the peak of the distributions, and again too many with very high values. A change in the Λ value does not result in better overall agreement. It might be that the two fragmentation schemes, string breaking and cluster decays, used successively in this model lead to a higher probability of extreme event shapes. The particle and energy flow (Figs. 25 and 26) are more populated around 20° and less in the region perpendicular to the sphericity axis.

For the rapidity (Fig. 24) the model predicts rather a deeper dip at $y=0$ and a higher peak at $y \simeq 1.5$. It is interesting that the rapidity distributions for the four models look quite different close to zero. Although all three parton-shower models take the interference effects into account, they give different predictions for the form of the dip. Problems similar to those described here have also been found in comparisons with other published data by the authors of the model.[7]

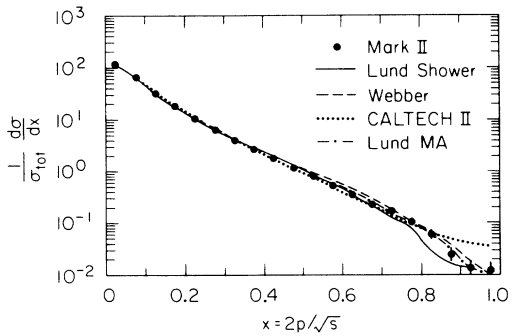

FIG. 23. The charged-particle x distribution in comparison with the models.

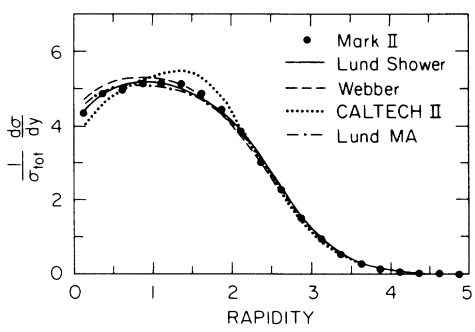

FIG. 24. The rapidity distribution of charged particles with respect to the thrust axis in comparison with the models.

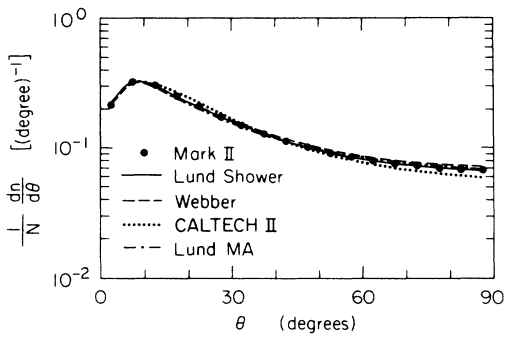

FIG. 25. The charged-particle flow with respect to the sphericity axis in comparison with the models.

Trying to understand the problems of the CALTECH II model, we implemented the Lund parton shower or the Lund fragmentation in the CALTECH II model. The combination of the CALTECH II parton shower with the Lund string fragmentation improved the agreement with the data, but, for example, the higher rates with very low and high thrust still remain, indicating that some of the problems, in particular the overestimation of the number of nearly spherical events, originate in the CALTECH II parton-shower model. One surprising feature of the model is that the average number of final quarks of 2.73 is roughly as large as the number of gluons with 2.69 per event in the parton shower.

The use of the Lund parton shower with the CALTECH II hadronization results in better agreements than the previous combination. For this combination the resulting distribution at low thrust describes the data reasonably well, but the peak at high thrust is still shifted to higher values than measured. Other distributions also indicate that the hadronization of the partons does not seem to be broad enough for pencil-like jets.

The new version of the Webber model gives a good reproduction of the data in Q_2-Q_1 (Fig. 11) which are quite sensitive to hard-gluon radiation. The older version 2.0 substantially underestimated the high Q_2-Q_1 tail. The new version still overestimates the number of events with high thrust, low minor value, low $M_{\rm br}^2/s$,

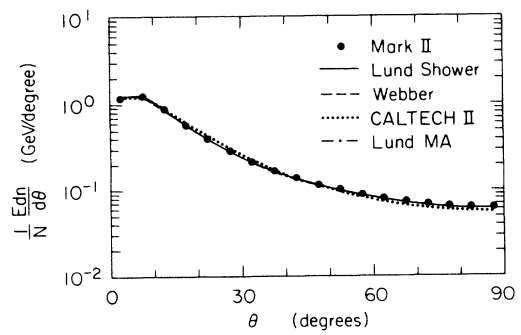

FIG. 26. The energy flow with respect to the sphericity axis in comparison with the models.

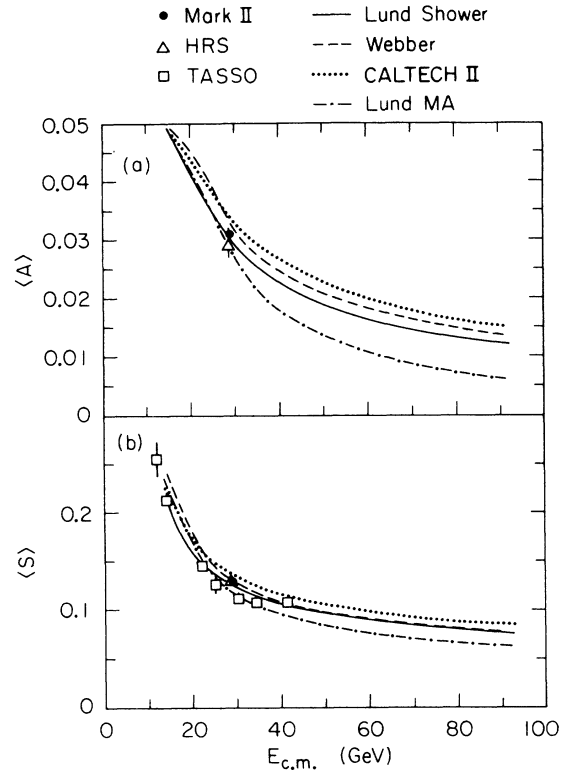

FIG. 27. (a) The ⟨aplanarity⟩ and (b) ⟨sphericity⟩ as a function of $E_{c.m.}$ in comparison with HRS and TASSO results and the model predictions.

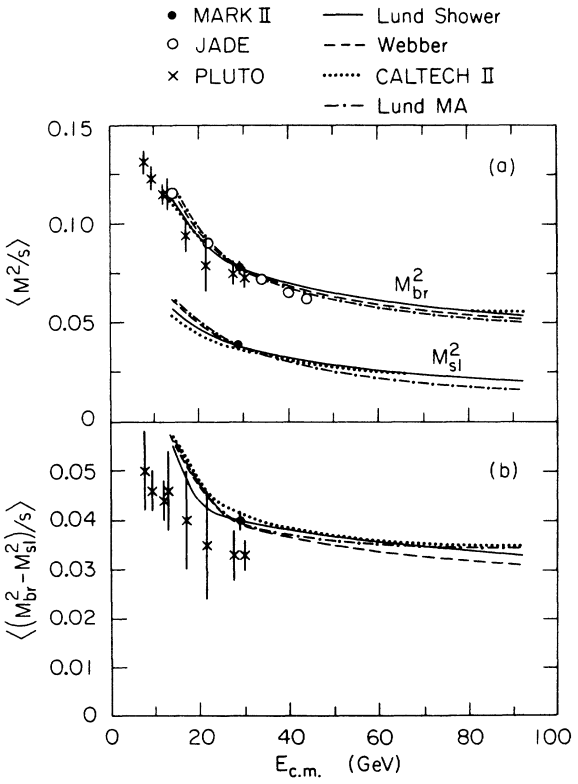

FIG. 28. (a) The $\langle M_{\rm br}^2/s\rangle$ and $\langle M_{\rm sl}^2/s\rangle$, and (b) $\langle (M_{\rm br}^2-M_{\rm sl}^2)/s\rangle$ as a function of $E_{c.m.}$ in comparison with PLUTO and JADE results and the model predictions.

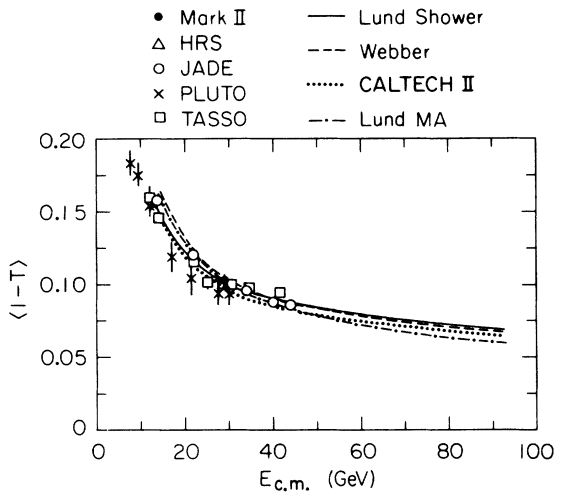

FIG. 29. The $\langle 1-T \rangle$ as a function of $E_{c.m.}$ in comparison with HRS, JADE, PLUTO, and TASSO results and the model predictions.

low M_{sl}^2/s (Figs. 13, 14, 16, and 17) and low multiplicity (not shown), probably because of insufficient soft-gluon radiation. Lowering the cutoff mass in the parton shower would increase the number of gluons, but would also lower the final multiplicity, again a problem of the special handling of heavy cluster decay. The average $p_\perp^2$ (Fig. 19) is slightly too high and the inclusive x distribu-

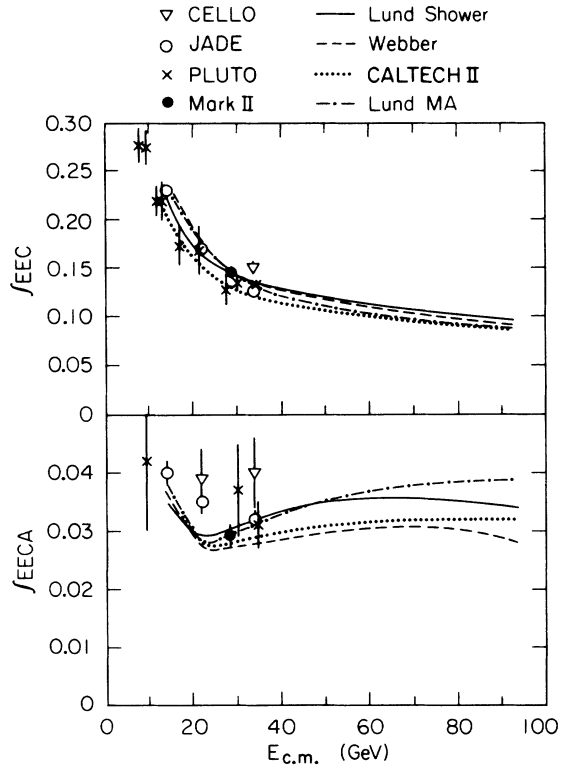

FIG. 30. (a) The energy-energy correlation (EEC) integrated in the angular region $57.6° < \theta < 122.4°$ and (b) the asymmetry of EEC integrated in the angular region $28.8° < \theta < 90°$ as a function of $E_{c.m.}$ in comparison with CELLO, JADE, and PLUTO results and the model predictions.

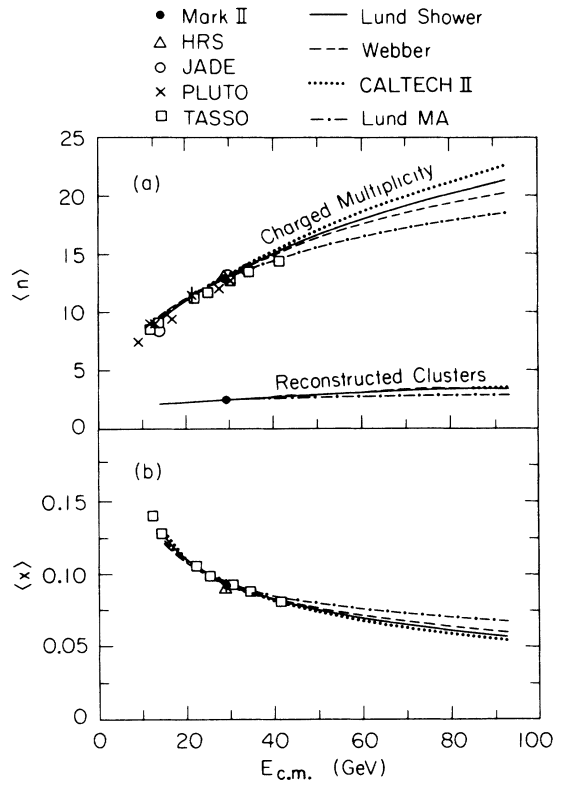

FIG. 31. (a) The mean multiplicity and number of reconstructed jets or clusters and (b) the mean charged-particle x as a function of $E_{c.m.}$ in comparison with HRS, JADE, PLUTO, and TASSO results and the model predictions.

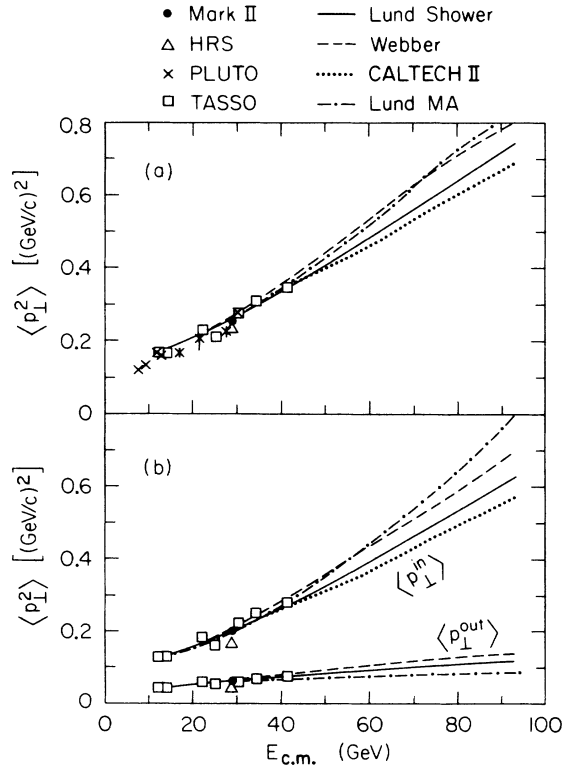

FIG. 32. (a) The $\langle p_\perp^2 \rangle$ and (b) the $\langle (p_\perp^{out})^2 \rangle$ and $\langle (p_\perp^{in})^2 \rangle$ as a function of $E_{c.m.}$ in comparison with HRS, PLUTO, and TASSO results and the model predictions.

TABLE XX. The rapidity distribution, $(1/\sigma_{tot})d\sigma/dy$ (folded around $y=0$).

Rapidity	Data averaged	PEP 5 detector	Upgraded detector
0.00–0.25	4.35±0.058	4.42±0.062	4.23±0.081
0.25–0.50	4.86±0.071	4.87±0.074	4.85±0.093
0.50–0.75	4.96±0.080	4.99±0.082	4.92±0.10
0.75–1.00	5.14±0.092	5.10±0.092	5.18±0.11
1.00–1.25	5.16±0.097	5.16±0.098	5.15±0.11
1.25–1.50	5.12±0.097	5.14±0.099	5.10±0.11
1.50–1.75	4.88±0.093	4.93±0.096	4.83±0.11
1.75–2.00	4.42±0.086	4.36±0.086	4.50±0.10
2.00–2.25	3.86±0.075	3.87±0.077	3.84±0.092
2.25–2.50	3.03±0.061	2.96±0.061	3.13±0.078
2.50–2.75	2.24±0.067	2.20±0.067	2.31±0.084
2.75–3.00	1.48±0.046	1.47±0.046	1.49±0.059
3.00–3.25	0.930±0.031	0.917±0.031	0.953±0.041
3.25–3.50	0.530±0.019	0.535±0.020	0.521±0.025
3.50–3.75	0.279±0.014	0.279±0.014	0.279±0.019
3.75–4.00	0.138±0.010	0.134±0.010	0.148±0.015
4.00–4.25	0.057±0.006	0.059±0.007	0.055±0.008
4.25–4.50	0.023±0.003	0.023±0.003	0.024±0.005
4.50–4.75	0.010±0.002	0.011±0.002	0.009±0.002
4.75–5.00	0.004±0.001	0.004±0.001	0.003±0.001

tion (Fig. 23) lies above the data for large x. The sum of χ^2 is 2870, which is half way between the Lund model and the CALTECH II model.

To see whether these problems come more from the parton-shower scheme of the model or the hadronization, we used only the parton shower of the Webber model. Instead of breaking each gluon into a $q\bar{q}$ pair, the Lund string was stretched from a quark via the gluons to the antiquark and this string then fragmented according to the Lund model. With this scheme we achieved much better agreement with the data (roughly as well as with the Lund shower model) than with the original version. But the cutoff for further parton evolution (m_g) has then to be reduced to 0.6 GeV, the lowest possible value for the generator. These factors indicate that the problems in the Webber model may be due more to the hadronization side.

The Lund shower model gives one of the best descriptions of the data, indicated by the sum of χ^2 of 960 which is the lowest value of the models used. There are still some slight deviations in a few distributions, but they are usually on the order of the differences between our data and the results from other experiments. There are some slight underestimations in the Q_x thrust, and M_{br}^2/s distributions (Figs. 10, 13, and 16) close to the peak values, and the x distribution (Fig. 23) is somewhat higher around $x=0.5$.

The branching ratios of the decaying D^0 and D^+ reflect visibly on the observed distributions. We used slightly different decay modes and branching ratios than were originally in the version JETSET 6.3, taking into account some of the later Mark III measurements.[15] With the original version, a change of the parameters A from 0.45 to 0.5 and σ_q from 230 to 250 MeV is necessary to get similar agreement with the data using the different D decay probabilities.

An interesting point is that a low cutoff mass in the parton shower ($Q_0 \sim 1.0$ GeV) is needed to describe the

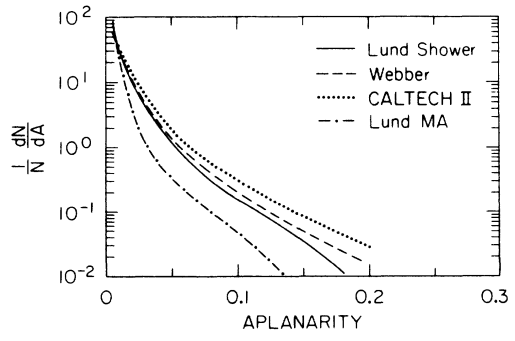

FIG. 33. The predicted aplanarity of the models at $E_{c.m.}=93$ GeV.

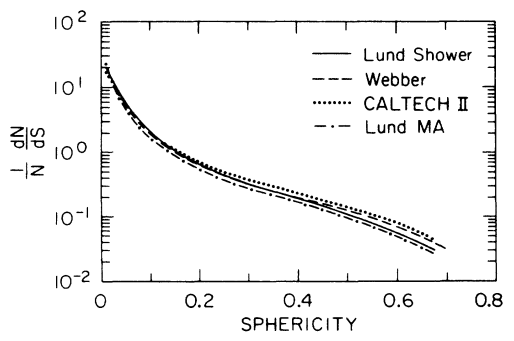

FIG. 34. The predicted sphericity of the models at $E_{c.m.}=93$ GeV.

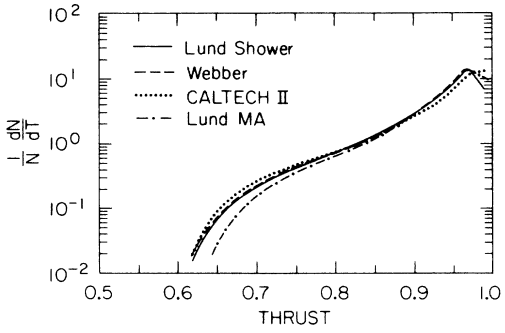

FIG. 35. The predicted thrust of the models at $E_{\text{c.m.}}=93$ GeV.

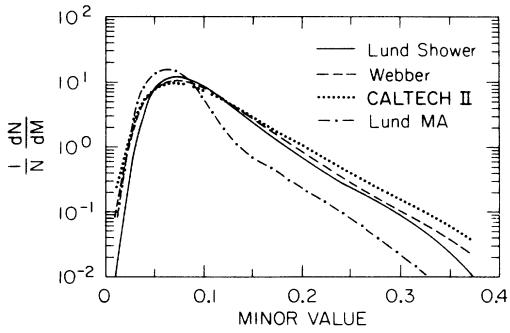

FIG. 36. The predicted minor distribution of the models at $E_{\text{c.m.}}=93$ GeV.

data around the peaks in the global shape distributions. It indicates that multiple-gluon radiation within an event is important even in connection with string fragmentation, to get a good transition between the perturbative and nonperturbative part.[33] An average of 4.8 gluons and 2.1 quarks are produced in the parton shower with the given parameters and only 3% (3%) of the events have no (one) gluon radiated.

IX. COMPARISON OF ENERGY BEHAVIOR OF OBSERVABLES

The description of the data by the models at a given c.m. energy is only one check of the underlying assumptions. Another check is whether the models can give the right prediction of the energy behavior of the data without changing the parameters. In relation to the upcoming Z^0 physics, it is interest to look at the extrapolation of the models to the 90-GeV region. As a first step we will look at the behavior of the average values of the observables. To increase the sensitivity, we also include published results of the PLUTO,[34] TASSO,[31] CELLO,[35] JADE,[14,36] and HRS[32] Collaborations. The average values for some of the observables from the previous section are given in Figs. 27–32 as a function of $E_{\text{c.m.}}$. The reader should keep in mind that the models are optimized to the Mark II points such that deviations between other measurements and the models may occur.

For the average aplanarity, in Figs. 27(a), the results from HRS and our measurement differ slightly. The four models all agree at very low $E_{\text{c.m.}}$, but at high $E_{\text{c.m.}}$ the Lund MA model predicts a factor of 2 lower value than the parton-shower models, again because of the incomplete simulation of multiple-gluon emission. However, the shower-model predictions also differ substantially. The average sphericity [Fig. 27(b)] of HRS and Mark II agree well, whereas TASSO measures lower values around 30 GeV. All models follow the trend of the data,

TABLE XXI. The charged-particle flow with respect to the sphericity axis, $(1/N)dn/d\theta$.

θ (deg)	Data averaged	PEP 5 detector	Upgraded detector
0.0– 5.0	0.213±0.002	0.210±0.002	0.217±0.003
5.0–10.0	0.326±0.003	0.322±0.003	0.333±0.004
10.0–15.0	0.305±0.003	0.302±0.003	0.309±0.004
15.0–20.0	0.254±0.005	0.252±0.005	0.258±0.006
20.0–25.0	0.210±0.004	0.208±0.004	0.213±0.005
25.0–30.0	0.172±0.003	0.172±0.003	0.172±0.004
30.0–35.0	0.147±0.003	0.148±0.003	0.146±0.003
35.0–40.0	0.126±0.002	0.129±0.002	0.122±0.003
40.0–45.0	0.114±0.002	0.115±0.002	0.112±0.003
45.0–50.0	0.099±0.002	0.101±0.002	0.097±0.002
50.0–55.0	0.090±0.002	0.091±0.002	0.089±0.002
55.0–60.0	0.084±0.002	0.083±0.002	0.085±0.002
60.0–65.0	0.079±0.001	0.080±0.002	0.078±0.002
65.0–70.0	0.076±0.002	0.076±0.002	0.076±0.002
70.0–75.0	0.072±0.002	0.073±0.002	0.072±0.002
75.0–80.0	0.069±0.002	0.069±0.002	0.069±0.002
80.0–85.0	0.069±0.002	0.070±0.002	0.067±0.002
85.0–90.0	0.067±0.002	0.068±0.002	0.064±0.002
$\langle\theta\rangle$ (deg)	31.7±0.6	31.9±0.6	31.4±0.6

TABLE XXII. The energy flow with respect to the sphericity axis, $(1/N)E\,dn/d\theta$.

θ (deg)	Data averaged	PEP 5 detector	Upgraded detector
0.0– 5.0	1.17±0.018	1.16±0.018	1.18±0.020
5.0–10.0	1.25±0.018	1.23±0.018	1.27±0.021
10.0–15.0	0.867±0.013	0.866±0.013	0.869±0.015
15.0–20.0	0.580±0.009	0.580±0.009	0.578±0.010
20.0–25.0	0.400±0.006	0.404±0.007	0.394±0.007
25.0–30.0	0.285±0.005	0.287±0.005	0.282±0.005
30.0–35.0	0.215±0.004	0.217±0.004	0.213±0.004
35.0–40.0	0.171±0.003	0.174±0.003	0.166±0.003
40.0–45.0	0.139±0.002	0.140±0.002	0.137±0.003
45.0–50.0	0.114±0.002	0.117±0.002	0.108±0.003
50.0–55.0	0.100±0.002	0.103±0.002	0.097±0.003
55.0–60.0	0.087±0.002	0.088±0.002	0.086±0.003
60.0–65.0	0.080±0.002	0.081±0.002	0.079±0.002
65.0–70.0	0.075±0.002	0.075±0.002	0.074±0.002
70.0–75.0	0.070±0.001	0.072±0.002	0.068±0.002
75.0–80.0	0.066±0.001	0.066±0.001	0.065±0.002
80.0–85.0	0.064±0.002	0.066±0.002	0.059±0.002
85.0–90.0	0.063±0.002	0.066±0.002	0.059±0.002
$\langle\theta\rangle$ (deg)	20.1±0.6	20.2±0.6	19.8±0.6

although Lund MA gives a lower extrapolation to higher $E_{c.m.}$. The experimental $\langle M_{br}^2/s\rangle$ [Fig. 28(a)] agree relatively well, and the models themselves follow the trend of the data fairly well. The $\langle (M_{br}^2-M_{sl}^2)/s\rangle$ value [Fig. 28(b)] of our measurement is substantially higher than those of PLUTO which is due to the fact that they calculate the two masses by a minimization process whereas we use the sphericity axis to define the two masses for both our data and the models. The models predict different slopes at higher energies. The three shower models give the same prediction around 70 GeV but diverge at 90 GeV. The values of $\langle 1-T\rangle$ (Fig. 29) of the different measurements scatter substantially. The models again predict quite different curvatures.

For Figs. 30(a) and 30(b), the energy-energy correlations[37] (EEC) and their asymmetry (EECA) have been calculated. Figure 30(a) shows the integral of the EEC from 57.6° to 122.4°. The agreement of the data points is fairly good. The CALTECH II model has lower values over the whole energy range than the Lund shower and the Webber model. Reference 7 claims this is because of the neglect of nonleading higher-order corrections in the leading-logarithmic shower formalism.

The energy behavior of the integrated EECA from 28.8° to 90° [Fig. 30(b)] is not very conclusive from the experimental point of view. On the other hand, it is interesting to see the different energy behavior of the models. The data look rather flat, but all four models decrease with energy until $E_{c.m.}\approx 20$ GeV, due to a nonvanishing contribution from the fragmentation of nearly 2-jet events. Above 20 GeV the Lund MA model predicts a continual increase up to 100 GeV. (A model with the same matrix elements to second order in α_s but with independent fragmentation leads to a decrease of the value over the whole region from 10 to 100 GeV, which is naively expected from the running coupling be-

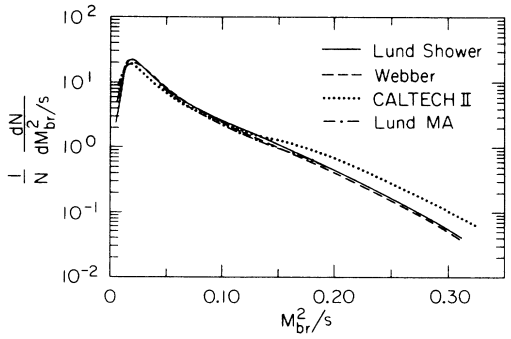

FIG. 37. The predicted M_{br}^2/s distribution of the models at $E_{c.m.}=93$ GeV.

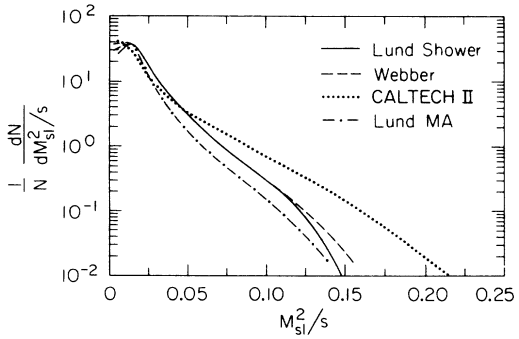

FIG. 38. The predicted M_{sl}^2/s distribution of the models at $E_{c.m.}=93$ GeV.

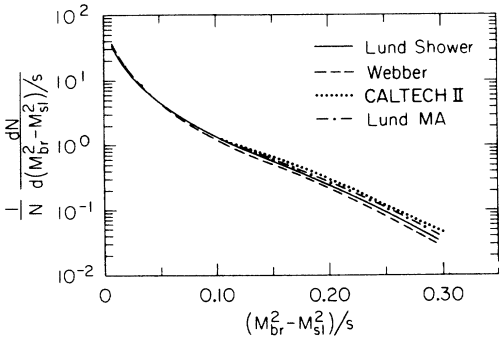

FIG. 39. The predicted $(M_{\rm br}^2-M_{\rm sl}^2)/s$ distribution of the models at $E_{\rm c.m.}=93$ GeV.

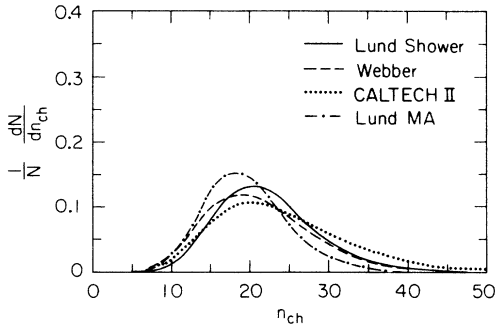

FIG. 41. The predicted multiplicity of the models at $E_{\rm c.m.}=93$ GeV.

havior of QCD.) The increase of Lund MA comes mainly from the decreasing power of the string effect with increasing energy. Fewer particles are produced between the quark and antiquark jets than between the quark and gluon jets in 3-jet events. These events look more 2-jet-like and hence have less asymmetry. With increasing jet energies the string effect becomes less pronounced, leading to a larger asymmetry. So the energy dependence of the EECA in the Lund MA model behaves oppositely to what one expects naively from the running coupling constant behavior in QCD. The asymmetries of the parton-shower models also increase after a dip at 20 GeV, until they reach a slight maximum between 60 and 80 GeV, after which they decrease again. One reason for this might be that events with multiple-gluon emission again look more symmetric, decreasing the value of asymmetry.

The average multiplicity in Fig. 31(a) shows good agreement at the existing energies with all four models, but the differences at high energies are such that their predictions at 90 GeV vary between 18 and 23 charged particles. The average number of reconstructed jets or clusters,[38] also shown in Fig. 31(a), has a nearly linear increase with $E_{\rm c.m.}$ for the shower models. The Lund MA model increases more slowly, predicting a value at the Z^0 which is 20% lower. As a direct correlation, the same trend as in the multiplicity is visible in Fig. 31(b), where the average particle x is plotted. The agreement between the different data points is quite good.

The average $p_\perp^2$ in Fig. 32(a) shows fair agreement between the experiments. It is interesting to notice the different $p_\perp^2$ behavior of the models. All the models show an increase in $p_\perp^2$ with energy, but the increase is less rapid for the Lund shower and CALTECH II than for the Webber model and Lund MA. This is probably partly due to the fact that the last two have a smaller multiplicity. The Lund MA prediction in Fig. 32(b) indicates that the increase in $p_\perp^2$ is not coming from $(p_\perp^{\rm out})^2$ which has the lowest increase with energy of all, but from $(p_\perp^{\rm in})^2$ which is mainly due to hard-gluon radiation.

Overall, the comparison of the average values of observables between the different experiments is satisfying. The largest deviations between experiments are in the aplanarity, sphericity, and $1-T$ distributions. The biggest difference in the energy behavior between the models is between the Lund MA model on the one hand and the shower models on the other hand.

X. PREDICTION OF THE MODELS AT THE Z^0

The figures in the previous section have already presented the average values of the observables at the Z^0

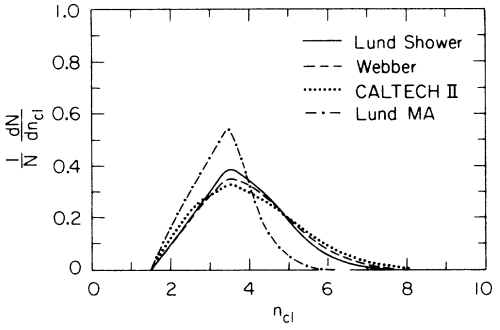

FIG. 40. The predicted number of reconstructed jets or clusters of the models at $E_{\rm c.m.}=93$ GeV.

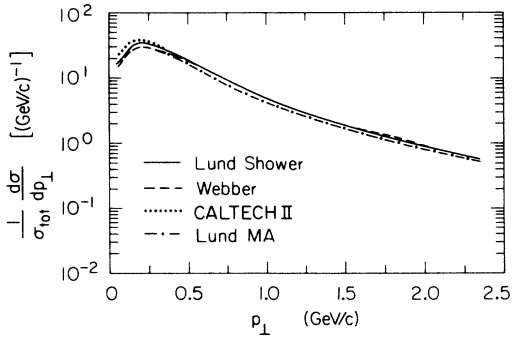

FIG. 42. The predicted $p_\perp$ distribution of charged particles with respect to the sphericity axis of the models at $E_{\rm c.m.}=93$ GeV.

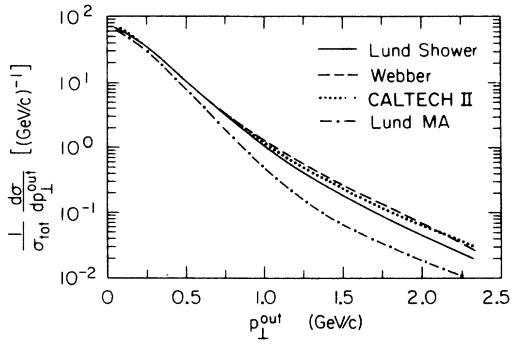

FIG. 43. The predicted $p_\perp^{out}$ distribution of charged particles with respect to the event plane of the models at $E_{c.m.}=93$ GeV.

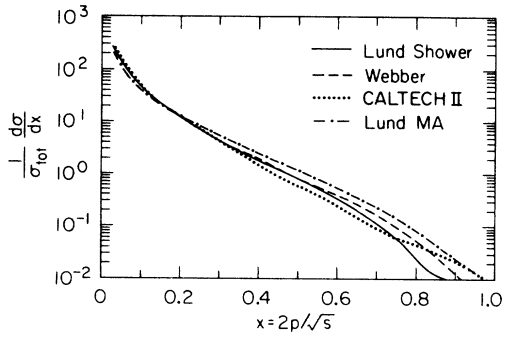

FIG. 45. The predicted charged particle x distribution of the models at $E_{c.m.}=93$ GeV.

energy. In Figs. 33–47 the distributions of the model predictions themselves are given for $E_{c.m.}=93$ GeV including the electroweak effects. Again, the same distributions are chosen as in the comparison at $E_{c.m.}=29$ GeV. The usual trend is that the global shape distributions peak more at low values, indicating that the events get narrower in width.

The aplanarity in Fig. 33 shows large differences between the models. This demonstrates that it might be dangerous to use a cut in aplanarity when looking for new particle production.[39] For Q_x, Q_2-Q_1, and sphericity the predictions differ only slightly: as an example, the sphericity is shown in Fig. 34. The CALTECH II model at 93 GeV again indicates for these observables the behavior of larger populations at very low and high values, and somewhat smaller in the medium range, in comparison with the other two shower models. The same trend is visible for thrust in Fig. 35. Events with low thrust are much more suppressed in the Lund MA model. The differences between the model predictions for the minor-value distribution in Fig. 36 are also visible at 93 GeV. The lack of multiple-gluon events makes the Lund MA curve much narrower than the other three. The differences between the Lund shower and Webber model are mainly due to differences in hadronization.

The M_{br}^2/s distribution in Fig. 37 again indicates the special form of the CALTECH II model which causes it to be a bit higher on the tail than the other three models. For M_{sl}^2/s in Fig. 38, the Lund shower and the Webber models give nearly the same prediction whereas the CALTECH II model is far higher in the tail and the Lund MA is visibly lower. All four models give similar predictions for $(M_{br}^2-M_{sl}^2)/s$ as shown in Fig. 39. Above a value of 0.12 the distributions at $E_{c.m.}=29$ GeV and 93 GeV nearly agree. This is expected if the tail is mainly sensitive to hard-gluon radiation.

The number of reconstructed clusters or jets in Fig. 40 shows a clear distinction between the second-order matrix element and the shower models. The shower models will drastically increase the predicted background in the top-quark search using jet reconstruction.[40] For the charged multiplicity in Fig. 41, CALTECH II indicates the broadest distribution, probably due to using both string breaking and cluster decay. This model says that events even with more than 50 charged particles are occasionally possible, in contrast with the other models which do not have this high of a multiplicity.

The $p_\perp$ distributions in Figs. 42–44 have similar trends for all models except the $p_\perp^{out}$ of the Lund MA, which is again lower. The particle x distributions in Fig. 45 reflect the difference in multiplicity. In comparison with the prediction at $E_{c.m.}=29$ GeV, the Lund MA with fixed y_{min} cutoff shows no scaling violation at high x. A scale-breaking effect of the order of 25% is visible, if the Lund MA is used with fixed invariant-mass cutoff

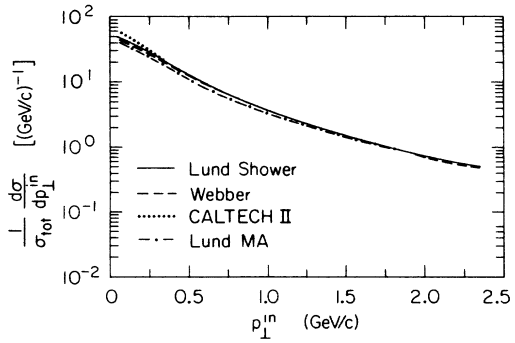

FIG. 44. The predicted $p_\perp^{in}$ distribution of charged particles to the sphericity axis in the event plane of the models at $E_{c.m.}=93$ GeV.

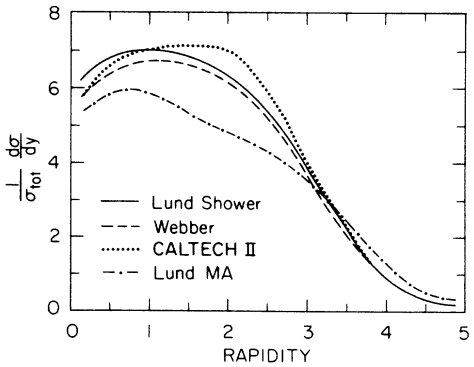

FIG. 46. The predicted rapidity distribution of charged particles with respect to the thrust axis of the models at $E_{c.m.}=93$ GeV.

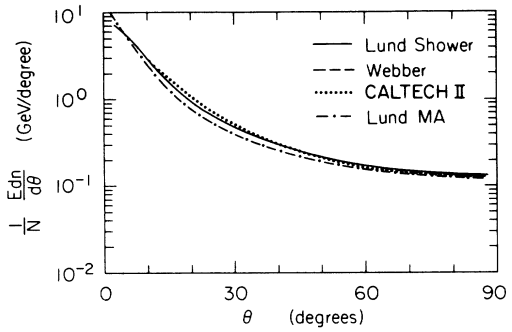

FIG. 47. The predicted energy flow with respect to the sphericity axis of the models at $E_{\text{c.m.}}=93$ GeV.

M_{ij}^2. The shower models predict a scaling violation of the order of 30%.

The different plateau heights in the rapidity distributions in Fig. 46 are due to the different multiplicities of the models. In addition they show quite different behavior in the plateau region and in their approach to the dip at $y=0$. A dip is predicted by both coherence effects on the parton level and by the string decay mechanism.

The energy flow in Fig. 47 emphasizes the difference between Lund MA and the shower models. The comparisons of the energy flow at $E_{\text{c.m.}}=29$ and 93 GeV show that for $\theta>15°$ the increase in energy is a factor of 2 over the whole region. The main increase in energy is in a cone of 10° around the sphericity axis.

Overall it is interesting to see that the three parton-shower models still give somewhat differing predictions at energies around 90 GeV. The differences which appear are often already visible at 30 GeV. A second-order matrix element model such as Lund MA is probably inadequate to describe data on the Z^0.

XI. SUMMARY

We have studied multihadronic events from e^+e^- annihilation at $E_{\text{c.m.}}=29$ GeV. The data were taken with the PEP 5 Mark II detector and the upgraded version of the detector. Event-shape distributions such as sphericity, thrust, and aplanarity, and inclusive particle distributions of such variables as x, rapidity $p_\perp$, and particle flow have been measured. The data corrected for detector acceptance from the PEP 5 detector and from the upgraded version agree within the errors.

The data corrected for acceptance and initial-state photon radiation are compared with different multihadron models, which use either second-order matrix element calculations or leading-logarithmic parton-shower evolution on the parton level, and string or cluster decay or a combination of both, for the hadronization. The new parton-shower models of Lund, Webber, and Gottschalk are improved compared to their older versions. They describe, for example, the aplanarity much better than the matrix element models. The lack of hard 3-jet events in the previous generation of parton-shower models has been eliminated in the new ones, which now give good descriptions for the Q_2-Q_1 distribution and the asymmetry of the energy-energy correlation. The Lund shower model gives the best description of the data. The CALTECH II model of Gottschalk and Morris still shows the largest deviations from the data.

The energy behavior of the shower models compared to average values of the observables also look quite reasonable. An extrapolation of the models to the 90-GeV region is presented. A model based on second order in α_s matrix element calculation plus fragmentation will probably be insufficient to describe the data in the 90-GeV region. The differences between the shower models are for most of the distributions of the same order of magnitude at 93 GeV as at 29 GeV. Those deviations which show up at 93 GeV and are already visible at 30 GeV might be eliminated by further improvement and tuning of the models to existing data.

ACKNOWLEDGMENTS

This work was supported in part by the Department of Energy under Contracts Nos. DE-AC03-81ER40050 (Caltech), DE-AA03-76SF00010 (University of California, Santa Cruz), DE-AC02-86ER40253 (University of Colorado), DE-AC03-83ER40103 (University of Hawaii), DE-AC02-84ER40125 (Indiana University), DE-AC03-76SF00098 (LBL), DE-AC02-84ER40125 (University of Michigan), and DE-AC03-76SF00515 (SLAC), and by the National Science Foundation (Johns Hopkins University).

[a]Present address: Universidad Autónoma de Barcelona, Bellaterra, Spain.
[b]Present address: University of Chicago, Chicago, IL 60637.
[c]Present address: Harvard University, Cambridge, MA 02138.
[d]Present address: University of Pennsylvania, Philadelphia, PA 19104.
[e]Present address: Therma-Wave Corporation, Fremont, CA 94539.
[f]Present address: University of California, Berkeley, CA 94720.
[g]Present address: Brookhaven National Laboratory, Upton, NY 11973.
[h]Present address: Vista Research Inc., 3600 Bayshore Road, Palo Alto, CA 94303.
[i]Present address: CERN, CH-1211, Genève 23, Switzerland.
[j]Present address: Laboratory für Hochenergie Physik Bern, CH-3012 Bern, Switzerland.
[k]Present address: Columbia University, New York, NY 10027.
[l]Present address: Université de Genève, CH-1211, Genève 4, Switzerland.
[m]Present address: University of Illinois, Urbana, IL 61801.
[n]Present address: Université Pierre Marie Curie, F-75230, Paris, France.
[o]Present address: Oxford University, Oxford, England.

[1]P. Hoyer *et al.*, Nucl. Phys. **B161**, 349 (1979); A. Ali *et al.*, Phys. Lett. **93B**, 155 (1980).
[2]B. Andersson *et al.*, Phys. Rev. **97**, 33 (1983).
[3]The first cluster model was from R. D. Field and S. Wolfram, Nucl. Phys. **B213**, 65 (1983).
[4]JADE Collaboration, W. Bartel *et al.*, Phys. Lett. **101B**, 129 (1981); **134B**, 275 (1984); H. Aihara *et al.*, Phys. Rev. Lett. **54**, 270 (1985).
[5]B. R. Webber, Nucl. Phys. **B238**, 492 (1984); (private communication).
[6]T. Sjöstrand, Comput. Phys. Commun. **39**, 347 (1986); T. Sjöstrand and M. Bengtsson, *ibid.* **43**, 367 (1987).
[7]T. D. Gottschalk and D. Morris, Nucl. Phys. **B288**, 729 (1987).
[8]G. Marchesini and B. R. Webber, Nucl. Phys. **B238**, 1 (1984).
[9]See, e.g., P. Dauncey, Ph.D. thesis, 1986.
[10]It should be noted that the "string" effect disappears in the Webber model if these large-mass clusters are allowed to decay isotropically.
[11]See also A. Petersen, in *Strong Interaction and Gauge Theories,* proceedings of the XXI Rencontre de Moriond, Les Arcs, France, 1986, edited by J. Tran Thanh Van (Editions Frontiéres, Gif-sur-Yvette, France, 1986), p. 291.
[12]G. Altarelli and G. Parisi, Nucl. Phys. **B216**, 298 (1977).
[13]The Lund model uses the calculations of F. Gutbrod, G. Kramer, and G. Schierholz, Z. Phys. C **21**, (1984) 235. These calculations lead to a $\simeq 10\%$ higher value of α_s than more recent calculations [see, e.g., G. Kramer and B. Lampe, Report No. DESY 86-119, 1986 (unpublished)]. Since it has mainly an effect on the value of the coupling constant and not on the shape of the distributions, we still used the old calculations.
[14]JADE Collaboration, W. Bartel *et al.*, Z. Phys. C **25**, 231 (1984); **33**, 23 (1986).
[15]Using the definition of the Lund model the values have to be multiplied by $\sqrt{2}$.
[16]The following branching ratios were used for the D^+ decay: $e^+\nu_e s_{\rm jet}\bar{d}_{\rm jet}$ (18.2%), $\mu^+\nu_\mu s_{\rm jet}\bar{d}_{\rm jet}$ (18.2%), $\bar{K}^0\rho^+$ (11.6%), $\bar{K}^{*0}\pi^+$ (2.7%), $\bar{K}^0\pi^+\pi^0$ (0.9%), $K^-\pi^+\pi^+$ (11.4%), $\bar{K}^0\pi^+\pi^+\pi^-$ (15.2%), $K^-\pi^+\pi^+\pi^0$ (6.4%), $\bar{K}^0\pi^+$ (4.1%), $\bar{K}^0K^+$ (1.3%), $\phi\pi^+$ (1.0%), $K^-K^+\pi^+$ (0.7%), $\bar{K}^{*0}K^+$ (0.6%), $\pi^-\pi^+\pi^+$ (0.5%), $\bar{K}^0\pi^+\pi^0\pi^0$ (3.2%), $u_{\rm jet}\bar{d}_{\rm jet}s_{\rm jet}\bar{d}_{\rm jet}$ (4.0%). The D^0 branching ratios were assumed to be $e^+\nu_e s_{\rm jet}\bar{u}_{\rm jet}$ (7.0%), $\mu^+\nu_\mu s_{\rm jet}\bar{u}_{\rm jet}$ (7.0%), $K^{*-}\pi^+$ (7.3%), $\bar{K}^0\pi^+\pi^-\pi^0$ (13.9%), $K^-\rho^+$ (12.8%), $K^-\pi^+\pi^-\pi^+$ (11.0%), $K^-\pi^+$ (5.4%), $\bar{K}^0\omega$ (3.9%), $\bar{K}^0\pi^0$ (4.0%), $\bar{K}^{*0}\pi^0$ (2.0%), $\bar{K}^0\eta$ (3.9%), $\bar{K}^0\pi^-\pi^+$ (1.9%), $\bar{K}^0\rho^0$ (1.7%), $K^-\pi^+\pi^0$ (1.5%), $\pi^-\pi^+\pi^-\pi^+$ (1.0%), $\pi^-\pi^+\pi^0$ (1.5%), $K^{*-}K^+$ (1.1%), K^-K^+ (1.1%), $\pi^-\pi^+$ (0.6%), $K^-\pi^+\pi^0\pi^0$ (5.4%), $u_{\rm jet}\bar{d}_{\rm jet}s_{\rm jet}\bar{u}_{\rm jet}$ (6.0%). In the above branching ratios, the notation $q_{\rm jet}$ stands for a jet initiated by a quark (or antiquark) of type q, and fragmented or recombined according to the standard Lund scheme, as described in Ref. 6.
[17]X. Artru and G. Mennessier, Nucl. Phys. **B70**, 93 (1974).
[18]R. H. Schindler *et al.*, Phys. Rev. D **24**, 78 (1981).
[19]G. S. Abrams, IEEE Trans. Nucl. Sci. **27**, 59 (1980).
[20]See, e.g., Report No. CALT-68-1015, 1983 (unpublished).
[21]G. Hanson, in *Proceedings of the Wire Chamber Conference: Recent Trends and Alternative Techniques,* Vienna, Austria, 1986, edited by W. Bartl, G. Neuhofer, and M. Regler [Nucl. Instrum. Methods **A252**, 343 (1986)].
[22]W. T. Ford *et al.*, Nucl. Instrum. Methods **A255**, 486 (1987).
[23]J. Haggerty, Mark II/SLC Report No. 137, 1986 (unpublished).
[24]J. D. Bjorken and S. J. Brodsky, Phys. Rev. D **1**, 1416 (1970); G. Hanson *et al.*, Phys. Rev. Lett. **35**, 1609 (1975); we used the definition from C. Berger *et al.*, Phys. Lett. **82B**, 449 (1979).
[25]S. Brandt *et al.*, Phys. Lett. **12**, 57 (1964); E. Farhi, Phys. Rev. Lett. **39**, 1587 (1977).
[26]A. De Rújula *et al*, Nucl. Phys. **B138**, 387 (1978). We used the algorithm described in Ref. 6.
[27]L. Clavelli and D. Wyler, Phys. Lett. **103B**, 383 (1981).
[28]This is an improved version with baryon production based on Ali *et al.* (Ref. 1).
[29]F. A. Berends and R. Kleiss, Nucl. Phys. **B178**, 141 (1981).
[30]This correction procedure assumes that the variables factorize. In the case of extreme correlations, this can lead to additional uncertainties.
[31]TASSO Collaboration, M. Althoff *et al.*, Z. Phys. C **22**, 307 (1984).
[32]HRS Collaboration, D. Bender *et al.*, Phys. Rev. D **31**, 1 (1985).
[33]See also T. Sjöstrand and M. Bengtsson, Phys. Lett. B **185**, 435 (1987).
[34]PLUTO Collaboration, C. Berger *et al.*, Z. Phys. C **28**, 365 (1985); **12**, 297 (1982); Phys. Lett. **95B**, 313 (1980).
[35]CELLO Collaboration, H. J. Behrend *et al.*, Z. Phys. C **14**, 95 (1982).
[36]JADE Collaboration, W. Bartel *et al.*, Z. Phys. C **20**, 187 (1983).
[37]C. Basham, L. Brown, S. Ellis, and S. Love, Phys. Rev. Lett. **41**, 1585 (1978).
[38]We use the cluster algorithm of Ref. 6.
[39]See, e.g., G. Hanson, in *Proceedings of the Second Mark II Workshop on SLC Physics* (SLAC Report No. 306, 1987).
[40]See, e.g., K. O'Shaughnessy, in *Proceedings of the Second Mark II Workshop on SLC Physics* (Ref. 39).